Microstructure-property relationships of novel ultra-high strength press hardening steels

Henri Järvinen[1]*, Mari Honkanen[1], Olli Oja[2], Martti Järvenpää[2], and Pasi Peura[1]

[1]Laboratory of Materials Science, Tampere University of Technology

P.O. Box 589, FI-33101 Tampere, Finland

[2]SSAB Europe Oy, Harvialantie 420, FI-13300, Hämeenlinna, Finland

[1*)] henri.jarvinen@tut.fi

Abstract

The industrial significance of micro alloyed martensitic steels manufactured via cold rolling, re-austenitization and quenching has been typically recognized as low. However, it is currently believed that micro alloying can improve the in-service properties of ultra-high strength press hardening steels. In this work, five 34MnB5 based steels were designed to address the role of Ti and V when combined with Cr or Mo. Microstructure-property relationships were analyzed after die-quenching and additional bake hardening (BH) heat treatment using advanced methods of microscopy, glow discharge optical emission spectroscopy, quasistatic tensile tests, and 3-point bending tests. Results indicate that both Ti and V can provide grain size refinement through the formation of stabile nano-sized precipitates. The BH treatment improved post-uniform elongation values, indicating a trend of improved ductility. However, the expected improvements in bendability were clearly confirmed only for two V micro alloyed steels with the alloying concepts of 0.3 Cr-0.15 V-0.03 Al-0.02 Ti-0.0020 B and 0.3 Mo-0.15 V-0.0060 N (without Al-Ti-B additions) (wt-%). Thus, it was discovered that micro alloying with V, when combined together

with either Cr or Mo, provides promising combination of mechanical properties as far as the austenitization parameters are appropriately controlled.

KEYWORDS: Press hardening; Bake hardening; Martensite; EBSD; TEM, mechanical behavior

1. Introduction

Demand for even lighter and safer vehicles has been a strong driving force for the development of novel ultra-high strength steels. At the meantime, the significance of a special group of steels, i.e., press-hardening boron steels (PHS), has rapidly increased [1]. Hot formed martensitic steels of 22MnB5 type, providing tensile strength around 1500 MPa, have enabled remarkable weight savings in passenger car bodies without compromising crash-worthiness [2]. Despite the achievements within the steel research, new and still tightening regulations on CO_2 emissions require constant development of alloys and manufacturing processes. Currently, there is a demand for novel PHS providing ultra-high tensile strength of around 2000 MPa [2]. That kind of steel grade would enable weight savings of about 30 % in comparison with standard 22MnB5 grades [2].

The strength of martensite can be controlled by adjusting the C content of the steel [3]. However, retaining an adequate ductility or toughness has turned out to be challenging with higher C content of around 0.35 % that is required to reach a requested tensile strength of 2000 MPa [4, 5]. Alternatively, steels of 0.28 C-3 Mn (wt-%) type have been investigated for the same strength level [6]. The concepts of ductility, toughness and crash behavior are, however, complex by nature. For instance, tensile behavior of martensitic steels does not satisfactorily describe the crash behavior of press-hardened anti-intrusion components [7]. Instead, the crash folding capacity depends strongly on materials ability to

allow strain localization in bending deformation [8]. This feature can be measured using 3-point bending tests following the specifications of automotive standard VDA 238-100 [7]. Currently, 3-point bending is a reckoned method for assessing the crash behavior of PHS [9].

The in-service properties of predominantly martensitic PHS are finalized in a so-called paint baking process, also known as bake hardening (BH) heat treatment, typically performed on the body-in-white components [10]. Gerber et al. [2] pointed out that the effect of this heat-treatment cycle needs to be taken into account when evaluating the crash behavior of PHS. To support this statement, our earlier study [11] indicated that a typical BH treatment of 170 ˚C (443 K)/20 min, leads to notable improvements in the fracture behavior of 34MnB5 steel. Dietchs et al. [12] reported improvements in the maximum bending angle for a novel PHS representing the same strength level with 0.34 % C. Recent studies [13, 14] have suggested that the maximum bending angle of uncoated PHS can be improved with the controlled decarburization of the surface, which tends to occur naturally if the austenitization step is carried out in the air atmosphere. Decarburization results in the formation of the soft ferritic subsurface layer that has improved ability to withstand strain localization in bending, while the tensile strength is not significantly decreased [13, 15].

Bian et al. [8] pointed out that the standard 22MnB5 grade was not originally developed to meet the requirements of the automotive industry. The scientists suggested a number of ways to improve the alloy desing and mechanical properties of hot formed martensitic steels. The improvements in mechanical behavior rely on the prior austenite grain size (PAGS) refinement with the aid of micro alloying elements [6, 16-18]. Moreover, reducing the amount and size of hard and coarse secondary phase particles such as TiN may be valuable [5, 16, 19, 20]. Another considerable property of PHS is materials resistance to hydrogen embrittlement, i.e., minimized risk for delayed cracking. Regarding this, the

effects of micro alloying and controlled formation of nano-sized micro alloy precipitates seem to be advantageous: in addition to the grain refining effect, small precipitates act as hydrogen trapping sites [16]. Previous studies [5, 6, 16, 21, 22] are consistent that the increased resistance to delayed cracking is attributed to the addition of micro alloying elements Nb, Ti or V. More interestingly, also fine Fe based carbides seem to have a desired effect on the hydrogen embrittlement [6, 21]. Hence, along with micro alloying, also the BH treatment may be utilised to improve steels resistance against delayed fracture.

Despite the undisputed development potential discussed above, the most important property of PHS is still an adequate hardenability. PHS are traditionally alloyed with 1.2-1.3 % of Mn along with 0.1-0.2 % of Cr. Mo, in turn, is not widely used, but is an appealing alloying element to be used in novel PHS, since it efficiently hinders ferrite transformation and synergistically increases the hardenability effect of B [23, 24]. In a general level, Mo improves tempering resistance of martensitic steels by reducing the diffusivity of C [16, 24]. Therefore, the role of Mo is worth studying with respect to more conventional Cr alloying. Furthermore, Mo may increase the grain boundary cohesion of high angle grain boundaries (HAGB) [25]. Consequently, the effect of Mo on the ductility of martensite, including a large amount of HAGB [26], is one issue to consider, especially when negative effects of Mn alloying has been addressed earlier [25] and recently also within the context of PHS [5, 22]. Therefore, replacing some amount of Mn with Mo can be considered as a promising alternative when aiming for ultra-high strength levels.

Even though the micro alloying of PHS has been suggested to bring in substantial improvements in properties, the effect of Ti and V on the mechanical properties is unclear and has not been comprehensively addressed elsewhere. The present study focuses on explaining the microstructure-property relationships of novel ultra-high strength PHS designed to reach ultra-high strength level of

2000 MPa. In addition, the effect of the BH heat treatment will be studied, especially when evaluating the 3-point bendability of PHS as an indicative value for the crash behavior.

2. Materials and methods

2.1 Test materials

The test materials comprised four boron-alloyed 34MnB5 based steels along with a non-boron alloyed 34MnB5 based steel manufactured in the laboratory. In addition, a commercial 34MnB5 grade (hereafter Ref) was included in the experiments. Ref was supplied as continuously annealed (CA), meaning that an additional annealing treatment had been carried out after cold rolling. The laboratory steels were manufactured at Swerea KIMAB Research Centre (Stockholm, Sweden). The melts were made in a vacuum furnace and cast into 2 kg ingots with a square section of 40 x 40 mm. The ingots in the length of about 120 mm were reheated to 1250 ˚C (1523 K), annealed for 60 min, and hot rolled to 3 mm thickness using a laboratory rolling mill at the University of Oulu (Finland). The finishing temperature of the hot rolling was 900 ˚C (1173 K). The hot rolling was followed by accelerated cooling down to 650 ˚C (923 K), after which the strips were slowly allowed to cool down to the room temperature in order to simulate the thermal cycle of the industrial coiling process. Later on, the sheets were cold rolled to the 1.5 mm final thickness. Hereafter, codes Steel A and B will be used when referring to the Cr alloyed laboratory steels. Respectively, codes Steels C, D, and E will be used when referring to the Mo alloyed steels. The codes and chemical compositions are listed in Table 1.

Table 1. Codes and chemical compositions (in wt-%) for the investigated steels.

Steel	Sheet thickness	C %	Si %	Mn %	Cr %	Mo %	V %	Ti %	Al %	B %	N %	Ti/N ratio
Ref	1.1 mm	0.35	0.26	1.30	0.15	0.01	0	0.029	0.033	0.0026	0.0033	8.8
A	1.5 mm	0.35	0.30	1.37	0.30	0	0	0.090	0.023	0.0022	0.0029	31.0
B	1.5 mm	0.34	0.30	1.37	0.30	0	0.144	0.020	0.024	0.0019	0.0036	5.6
C	1.5 mm	0.34	0.29	1.38	0.02	0.29	0	0.019	0.021	0.0019	0.0017	11.2
D	1.5 mm	0.34	0.30	1.36	0.02	0.30	0.146	0.020	0.028	0.0017	0.0033	6.1
E	1.5 mm	0.34	0.29	1.28	0.02	0.30	0.147	0.001	0.004	0.0001	0.0060	0.2

As expressed in Table 1, Steels B, C, and D were alloyed with a conventional Al-Ti-B concept, but using slightly reduced amount of Ti, i.e., approximately 0.020 %. Considering the chemical compositions and Ti/N stoichiometric ratio of 3.4 [27], all N should be combined with Ti to form TiN in Steels B-D. TiN is very stable, and thus known to precipitate at high temperatures (at around 1400 ˚C (1673 K)) already during casting [16, 28]. In turn, Steel E was simply deoxidized using the typical amounts of Si and Mn without normal Al addition and contained slightly higher amount of N on purpose. Thus, the precipitation of TiN (and AlN) were thought to be eliminated in Steel E, thus leaving a vast majority of N available for precipitation with V. Steel A was micro alloyed with hyperstoichiometric amount of Ti (0.09 %) in order to form Ti based micro alloy precipitates. Respectively, Steels B, D, and E were micro alloyed with V (approximately 0.15 %) to form V based micro alloy precipitates. Fig. 1 presents optical micrographs of the initial microstructures.

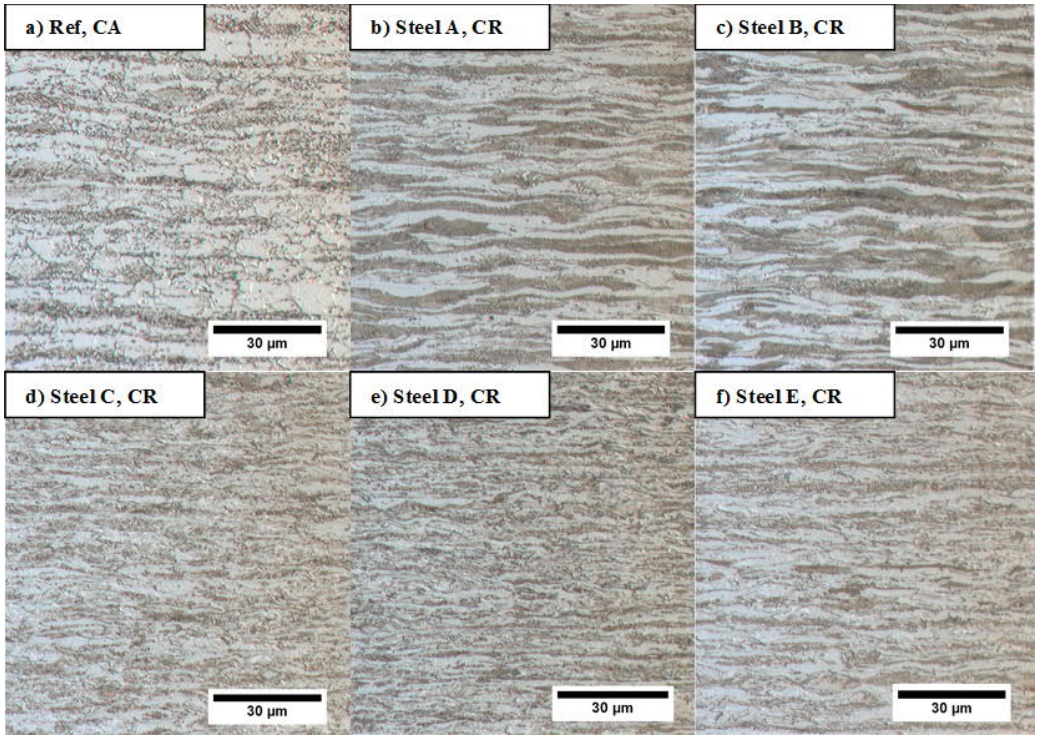

Fig. 1. Optical micrographs transverse to the rolling direction of the investigated steels; a) Ref; b) Steel A; c) Steel B; d) Steel C; e) Steel D; f) Steel E.

The optical micrographs (Fig. 1) reveal clear differences in the initial microstructures. The industrially produced reference grade Ref shows a partially recrystallized structure (Fig. 1a), meaning that the performed annealing step has also changed the pearlite morphology compared to the typical cold rolled structure seen in Steels A (Fig. 1b) and B (Fig. 1c). Accordingly, Steel A and B, consist primarily of ferrite and pearlite (Fig. 2a-c). Pearlite is seen in the form of large colonies together with elongated ferrite grains. The microstructures of Steels C, D, and E consists more preferably of finer constituents such as acicular ferrite and bainite with a small amount pearlite. From Steels C, D, and E, the amount of pearlite is highest in Steel E (Fig. 1f) most likely due to absence of B alloying. Mo is effective in preventing the formation of pearlite and instead promotes formation of bainite [29]. V, in turn, has been reported to promote the formation of acicular ferrite instead of pearlite, and thus to increase

hardenability of steel when it is in solution [30]. To sum up, it is evident that alloying concept controls the initial microstructure.

2.2 Press hardening experiments and bake hardening heat treatments

The cold rolled (CR) strip was cut into 100x60x1.5 mm sample sheets to be used in press hardening experiments. The experiments were carried out by using a custom-built press hardening equipment with a water-cooled flat-die. The details of the equipment have been described more specifically in an earlier study [31]. Two austenitization cycles designated as A_{c3}+60 s (~3 min) and A_{c3}+180 s (~5 min), in a constant furnace temperature of 900 ˚C (1173 K), were examined based on the required time to reach the austenite transformation temperature A_{c3}. The equation proposed by Kasatkin et al. [32] was chosen to calculate the A_{c3} temperatures for each steel. This procedure resulted in small differences in the total soaking times between the investigated steels as indicated in Table 2. The used definition allows unbiased comparison between the steels with different chemical compositions.

Table 2. Calculated A_{c3} temperatures and examined austenitization cycles of the press hardening experiments based on the time required to reach A_{c3} at a constant furnace temperature of 900 ˚C (1173 K).

Steel	A_{c3}	A_{c3}+60 s (~ 3 min)	A_{c3}+180 s (~ 5 min)
Ref	800 ˚C (1073 K)	172 s	292 s
A	812 ˚C (1085 K)	178 s	298 s
B	797 ˚C (1070 K)	172 s	292 s
C	813 ˚C (1086 K)	179 s	299 s
D	815 ˚C (1088 K)	180 s	300 s
E	809 ˚C (1082 K)	177 s	297 s

As measured, the temperature of the sheet was approximately 890 ˚C (1163 K) in the end of the shorter austenitization cycle of A_{c3}+60 s. However, in the case of prolonged cycle of A_{c3}+180 s, the target temperature of 900 ˚C (1173 K) was attained. After soaking, a sample was automatically transferred within 3 seconds to the die and subsequently quenched without deformation with 30 kN pressing force. A cooling rate of at least 80 ˚C/s was attained. The automated transfer mechanism ensured excellent repeatability of the experiments. After the press hardening experiments, another set of the die-quenched steel sheet samples were subjected to the BH heat treatment of 170 ˚C (423 K)/20 min. The heat treatment procedure was carried out following the specifications of EN 10325-2006 [33]. The procedure has been described more in detail in an earlier study [11].

2.4. Microstructure analysis

Metallographic samples in CR, PH, and PH+BH conditions were prepared with standard metallographic methods and etched using 4 % Nital solution. Systematic analysis with an optical microscope Nikon Eclipse MA 100 and a scanning electron microscope (SEM) Zeiss Ultra Plus equipped with energy dispersive X-ray spectrometer (EDS) INCAx-act silicon-drift detector, Oxford Instruments, were carried out. The SEM was fitted with a HKL Premium-F Channel electron backscatter diffraction (EBSD) system and a Nordlys F400 detector. EBSD analysis were performed for all steels and examined austenitization cycles to reveal prior austenite grain structures. The samples used in the EBSD measurements were final polished using colloidal silica suspension. The employed step size and acceleration voltage were 0.15 μm and 20 kV, respectively. The analyzed areas of 175×125 μm were located in one-third of the thickness of the sheet. Prior austenite grain boundary maps were reconstructed utilizing the EBSD data of martensitic microstructures. An algorithm script introduced by Nyyssönen et al. [34] was employed and reconstruction followed the methodology presented earlier in

190 [31]. Then, mean linear intercept method was used in the actual prior austenite grain size (PAGS)
191 determination as described earlier in [11]. Furthermore, the cross-sections used in the EBSD analysis
192 were additionally characterized with the SEM to determine the area fraction of coarse secondary phase
193 particles. A total of 40 SEM images (20 images from A_{c3}+60 s and 20 images from A_{c3}+180 s) with an
194 original magnification of 1000x were used to determine the area fraction of coarse particles/inclusions.
195 This resulted in the total spatial area of approximately 0.4 mm^2 per steel. An ImageJ image analysis
196 software [35] was used to threshold SEM images in order to separate the darker particles from the
197 brighter matrix. In addition, SEM-EDS analysis with the acceleration voltage of 15 kV were
198 simultaneously performed to roughly identify types of coarse secondary phase particles.
199
200 A transmission electron microscope (TEM) Jeol JEM-2010 equipped with an EDS detector Noran
201 Vantage Si(Li), Thermo Scientific, was used to analyze nano-sized precipitates from the PH steels. The
202 TEM samples were prepared from the micro alloyed Steels A, B, D, and E using an extraction replica
203 technique described specifically in [11]. For each sample, the size (diameter) of all identifiable
204 precipitates were determined from five TEM bright field (BF) images, which resulted in the analyzed
205 area of approximately 2 μm^2 per steel. In practice, precipitates smaller than 2 nm by diameter were
206 difficult to identify. In addition, EDS point measurements and selected area electron diffraction (SAED)
207 patterns were utilized to determine compositions and structures of the selected precipitates. In each case,
208 the employed acceleration voltage was 200 kV.
209
210 The samples used in 3-point bending tests (to be described in section 2.3) were also sectioned in order to
211 characterize the depth of decarburization. First, the thickness of a ferritic decarburization layer was
212 evaluated using optical micrographs. In addition, a GDA750 glow discharge optical emission
213 spectroscope Spectruma Analytik GmbH was used to measure the carbon concentration profiles from

surface down to the depth of approximately 50 μm. Duplicate measurements per sample were carried out with the sputtering diameter of 4 mm.

2.3. Mechanical tests

Tensile test specimens with a gauge length of 8.0 mm and width of 2.0 mm were water jet cut out of the hardened sheets. It can be mentioned that the measured total elongation values cannot be compared with the standard A80 values, but allow comparison between the steels used here. Three tensile specimens were prepared from each sample in both PH and PH+BH conditions. Quasistatic tensile tests were carried out at the strain-rate of 5×10^{-4} s^{-1} using a servo hydraulic materials testing machine Instron 8800 equipped with a 50 kN load cell. The elongation was measured using an extensometer with a 6 mm gauge length.

After die quenching, additional steel sheet samples in the standard size of 60x60x1.5 mm were prepared for 3-point bending tests to be examined in both PH and PH+BH conditions. The bending axis was transverse to the rolling direction. The bending tests were carried out following the specifications of VDA 100-238 by using a servo hydraulic materials testing machine MTS TestStar 810. Three parallel tests per steel were performed except in the case of Steel C (PH+BH) and Steel E (PH), in which only two successful tests were carried out. A bending fixture with low-friction support rolls (diameter 30 mm) and punch radius of 0.4 mm was used. A speed of 20 mm/min was used in bending tests. The bending angle at maximum force F_{max}, designated hereafter as α_{Fmax}, was calculated based on the geometry of the test-set up and measured force *vs.* displacement data as specifically described in VDA 100-238 [36].

3. Results

3.1. Transformed microstructures

Fig. 2 presents examples of the SEM micrographs for Steels C and E in both PH and PH+BH conditions, austenitized for A_{c3}+180 s/900 ˚C (1173 K). Based on the SEM analysis, predominantly martensitic microstructures were attained for all investigated steels in the case of both examined austenitization cycles of A_{c3}+60 s/900 ˚C (1173 K) and A_{c3}+180 s/900 ˚C (1173 K). In a general level, corresponding morphologies were observed in the case of all steels, and are not thus presented here thoroughly.

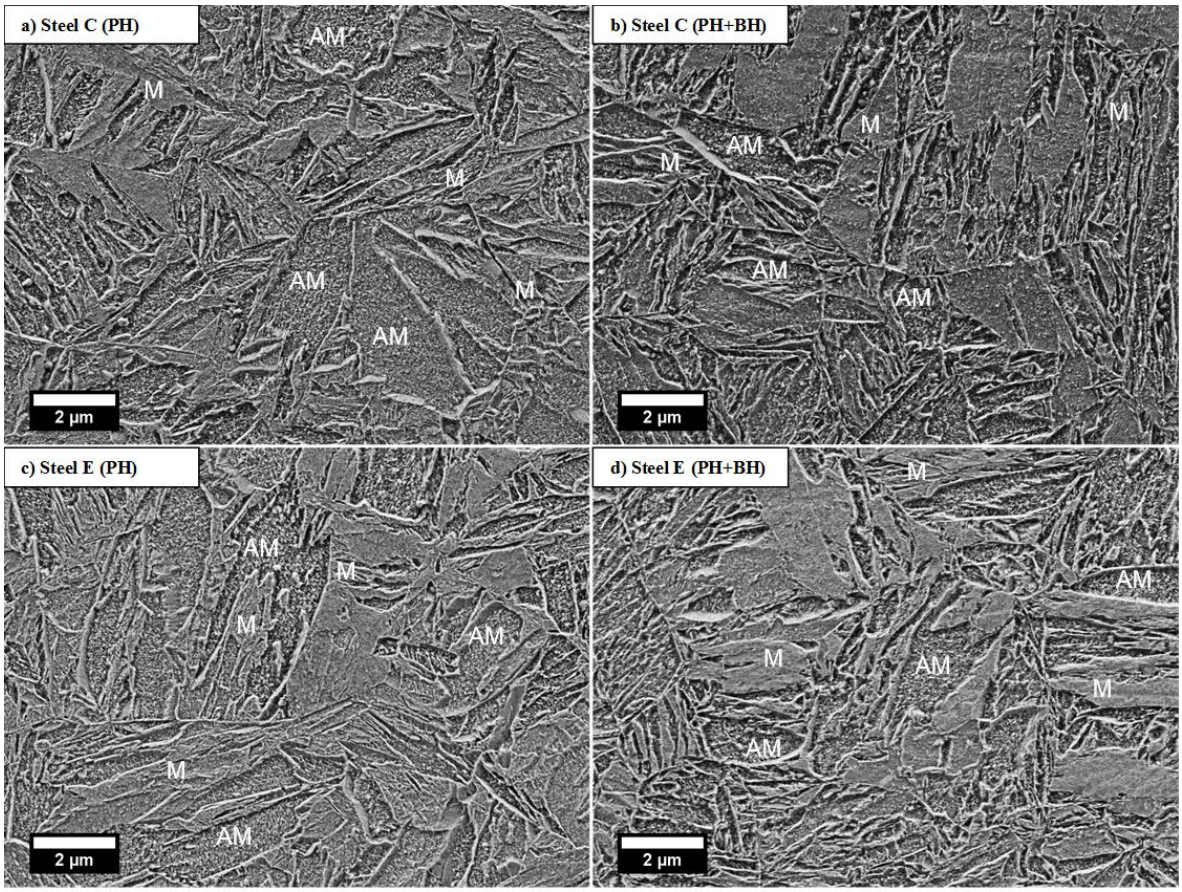

Fig. 2. Example SEM micrographs of Steel C in; a) PH and; b) PH+BH condition and Steel E in; c) PH and; d) PH+BH condition after austenitizing for A_{c3}+180 s at 900 ˚C (1173 K). The microstructures are mixtures of hard martensite (M) and auto-tempered martensite (AM).

In the PH condition (Fig. 2a and 2c), the microstructures consist of hard martensite (M) and auto-tempered martensite (AM). AM contains fine cementite precipitates (white dots in the SEM images) already in the PH state, while the regions of M are principally pure from cementite. The characteristics of auto-tempering has been discussed more in detail in our earlier studies [11, 31] and also by other researchers [37]. Thus, the auto-tempering, occurring for the time span of some seconds between approximately 400 ˚C (673 K) and 200 ˚C (473 K), causes the formation of fine cementite precipitates that are identifiable with SEM. In turn, the microstructural influence of the BH treatment is not that clear, but can be also observed from the increased amount and size of fine cementite precipitates in particular within the areas of hard martensite. Accordingly, the increased amount of fine cementite particles can be observed more clearly in Steel C (Fig. 2b), whereas in the case of Steel E (Fig. 2d) the same behavior is not obvious. This may be caused by local differences in microstructures and etching behavior, but can also depend on alloying. Understanding the role of alloying elements would require comprehensive TEM studies, and will be therefore left outside the scope of this study. The formation of very fine Fe based transition carbides should also occur during the BH treatment [38], but cannot be identified with the SEM analysis. It is believed that they are too fine to be seen with the resolution of SEM. However, evidence on the formation of transition carbides in the corresponding conditions has been presented earlier by other researchers for example in [39].

It has been reported [15] that surface decarburization promotes the formation of a soft ferritic subsurface layer and improves the 3-point bendability of martensitic PHS. Thus, the subsurface microstructures were characterized from the samples used in the 3-point bending tests. Fig. 3 presents representative optical micrographs from the subsurface regions of each laboratory steel after austenitizing for A_{c3}+180s

at 900 ˚C (1173 K). Ref is omitted here, since it was excluded in 3-point bending due to smaller sheet thickness.

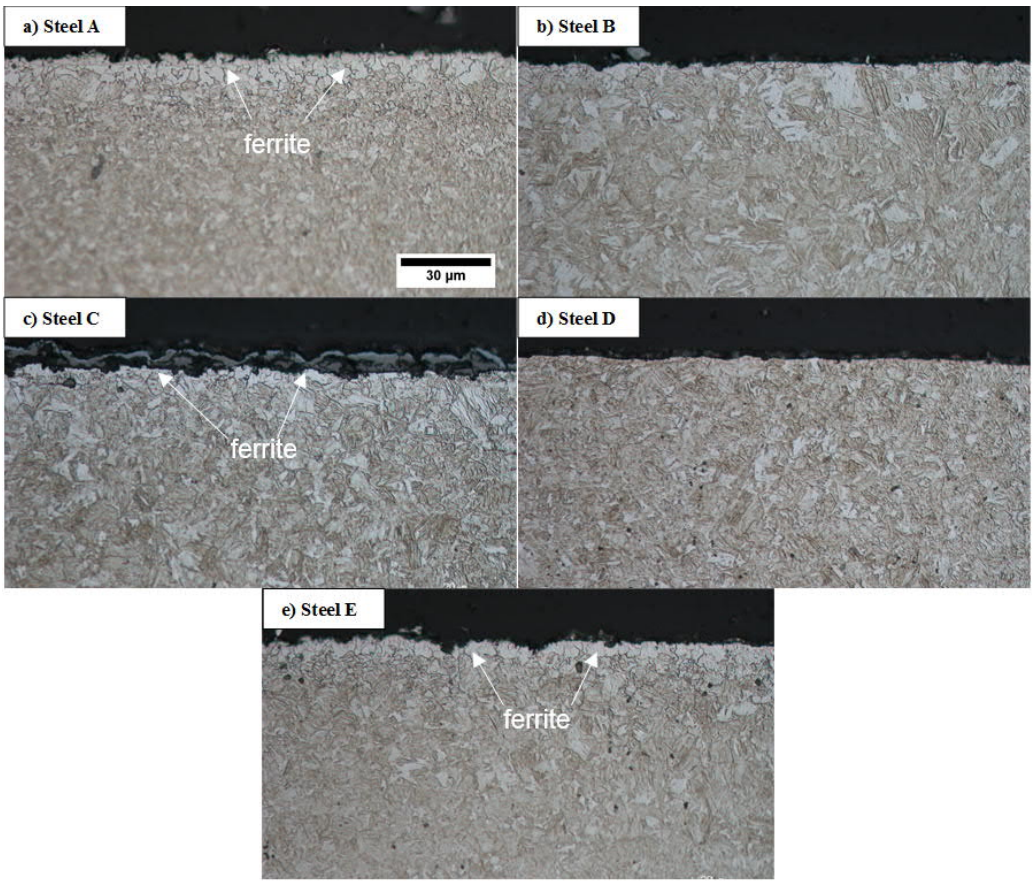

Fig. 3. Optical micrographs from the subsurface regions of the PH steels; a) Steel A; b) Steel B; c) Steel C; d) Steel D; e) Steel E after austenitizing for A_{c3}+180 s at 900 ˚C (1173 K). Steels A, B, C and E show ferritic phases on the surface, whereas the subsurface microstructure of Steel D is most preferably fully martensitic. The scale is the same in all images.

A ferritic layer with a thickness of approximately 10-30 µm has formed in Steels A (Fig. 3a) and E (Fig. 3e). However, Steels B (Fig. 3b) and C (Fig. 3c) show only small amount of ferrite in the vicinity of the surface. Steel D (Fig. 3d), in turn, do not show any ferritic phases and microstructure is predominantly martensitic even in the surface. It needs to be considered that the formation of ferritic layer depends on the chemical composition, which in turn controls the hardenability of steel. Therefore, local carbon

content and the amount of other alloying elements control the phase transformations. To create better understanding on the role of decarburization, carbon concentration profiles from surface towards sheet thickness centreline were determined. The measured GDOES profiles are presented in Fig. 4.

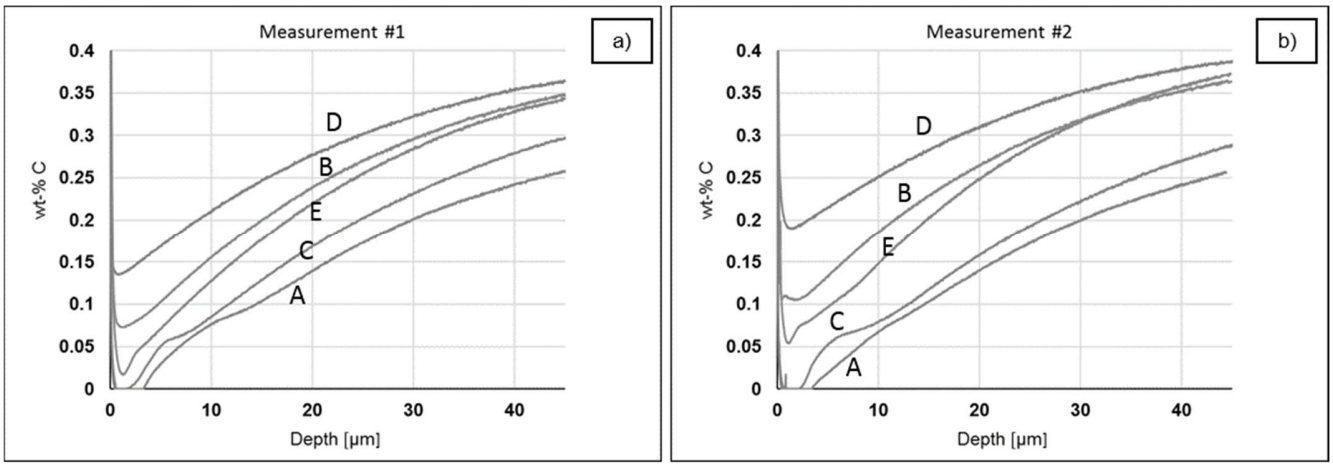

Fig. 4. Carbon concentration profiles; a) measurement #1; b) measurement #2 by GDOES for the laboratory Steels A-D measured from the surface of the 3-point bending samples (A_{c3}+180 s/900 ˚C (1183 K)) in the PH condition.

The graphs (Fig. 4) support the observations made on the basis on the optical micrographs (Fig. 3). Steels A, C, and E show the smallest carbon concentration in the subsurface region, whereas in Steels B and D the concentrations are much higher in the vicinity of the surface. In addition, the results suggests that also steel composition has affected the decarburization process, e.g., by controlling the oxide layer characteristics. The comparison of Fig. 4a and 4b, implies that there exists some scatter between the measurements. This may be caused by local compositional differences and small fluctuations in the surface topographies. However, the mutual order of steels is the same in both cases.

3.3. Prior austenite grain sizes

Fig. 5 presents examples of the reconstructed parent austenite grain boundary maps for Steels A and B. The maps show prior austenite grain boundaries (PAGB) as black lines. In addition, red and green lines show packet and block boundaries of martensite, respectively.

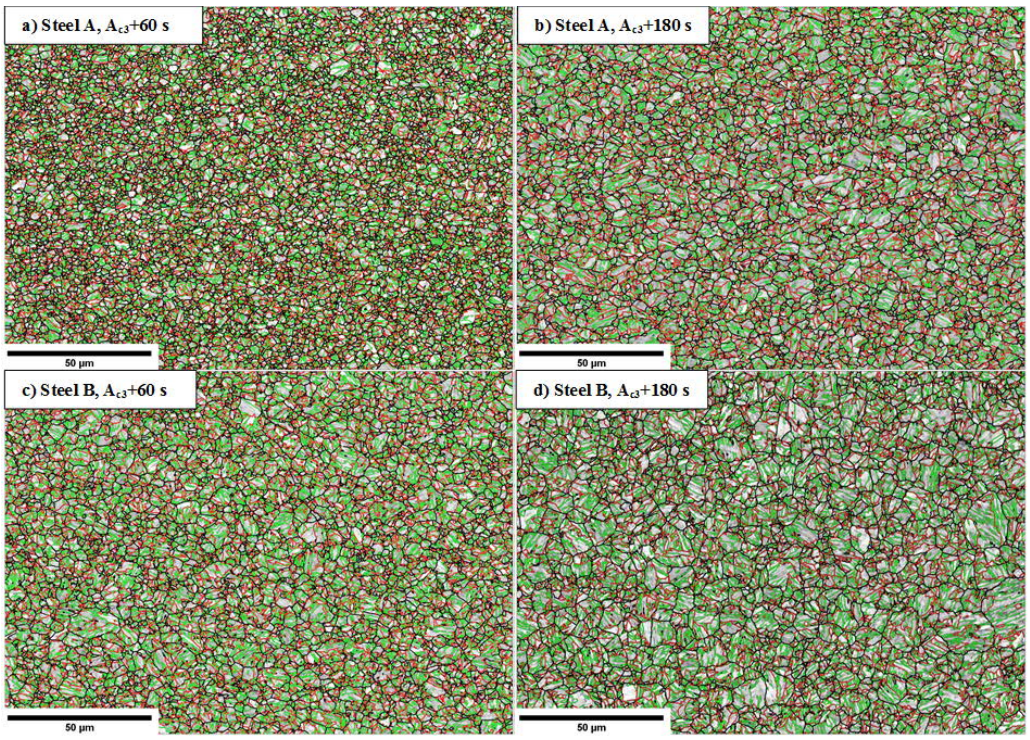

Fig. 5. Prior austenite grain boundary (PAGB) maps for Steel A austenitized for; a) A_{c3}+60 s; b) A_{c3}+180 s/900 ˚C (1173 K) and for Steel B austenitized for; c) A_{c3}+60 s; d) A_{c3}+180 s/900 ˚C (1173 K). The viewing direction is transverse to the original rolling direction. PAGB are superimposed on EBSD band contrast images as black lines, and the red and green lines show packet and block boundaries of martensite, respectively. (For interpretation of the references to color in this figure legend, the reader is referred to the web version of this article.)

The PAGB maps (Fig. 5) imply that the attained PAGS are very fine. In addition, a small increase in PAGS can be observed between the examined austenitization times. The grains are equiaxed indicating

that austenite has recrystallized during the examined austenitization cycles. Table 3 summarizes the measured PAGS for all investigated steels.

Table 3. Measured PAGS for the PH samples austenitized for A_{c3}+60 s and A_{c3}+180 s at 900 ˚C (1173 K). Designation ΔGS refers to the increase in PAGS between the studied austenitization cycles.

Steel	PAGS, (µm) – TD, A_{c3}+60s/900 °C	PAGS (µm) – TD, A_{c3}+180s/900 °C	ΔGS(µm) – TD
Ref	4.7 (±0.4)	5.6 (±0.7)	0.9
A	2.4 (±0.1)	3.8 (±0.3)	1.4
B	3.7 (±0.4)	5.4 (±0.6)	1.7
C	3.6 (±0.4)	4.5 (±0.6)	0.9
D	2.8 (±0.2)	3.9 (±0.4)	1.1
E	2.6 (±0.2)	6.0 (±0.8)	3.4

The measurement data confirms that the PAGS of laboratory Steels A-E are extremely fine especially after the shorter austenitization cycle of A_{c3}+60 s/900 ˚C (1173 K). The longer austenitization cycle of A_{c3}+180 s/900 ˚C (1173 K) has resulted only in the small increase in the PAGS designated here as ΔGS. As noted in Fig. 5, the most efficient PAGS refinement was achieved in Steel A alloyed with excess Ti. The PAGS of the other Cr alloyed Steel B (micro alloyed with V), are slightly larger. Almost equal PAGS has been attained also for Mo-alloyed Steels C and D. When comparing Steels C and D, the measured PAGS are slightly smaller in Steel D that was additionally micro-alloyed with V. In Steel E (micro alloyed with V), the measured PAGS is extremely small after the shorter austenitization cycle of A_{c3}+60 s/900 ˚C (1173 K), whereas the prolonged annealing of A_{c3}+180 s/900 ˚ (1173 K) has resulted in the most remarkable increase in the PAGS. As a sole, this has resulted in larger PAGS in comparison with Ref.

3.4. Coarse secondary phase particles and inclusions

The area fraction of coarse secondary phase particles were characterized from polished and unetched cross-sections. Fig. 6 presents example SEM images used in the analysis for a Steels A and C.

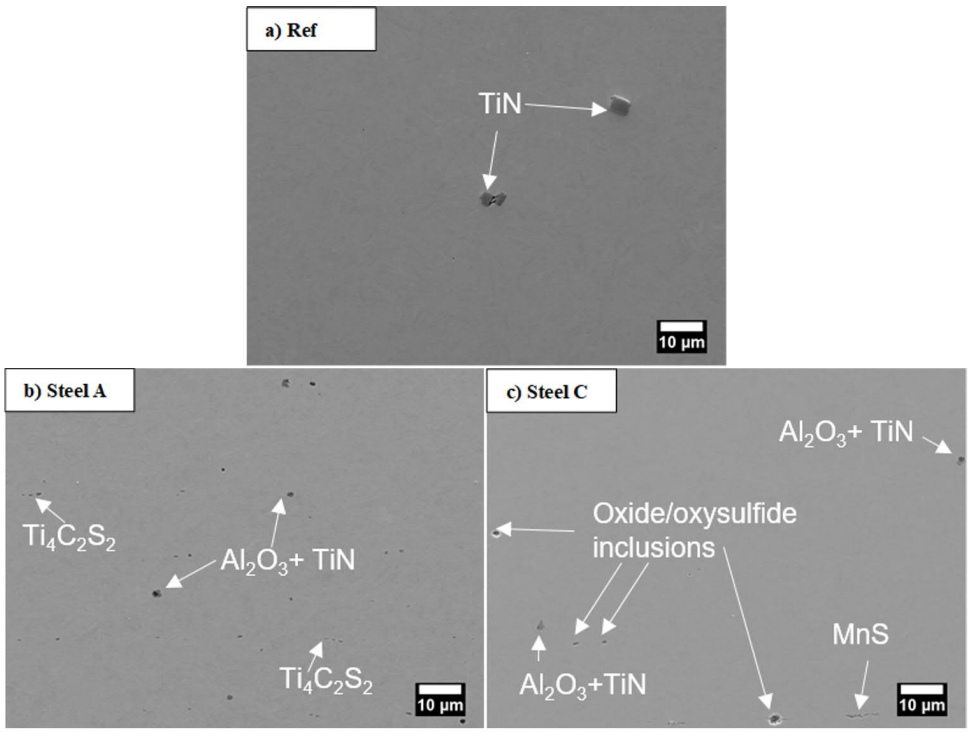

Fig. 6. Example SEM images of; a) Ref; b) Steel A; c) Steel C revealing secondary phase particles as darker from the brighter matrix.

Based on the present context and elemental information gathered with EDS, the secondary phase particles (or inclusions) were appraisingly identified. Table 3 summarizes the indicative results of the types of particles/inclusions. In addition, the calculated area fractions of all recognizable particles are presented.

Table 4. Types and determined area fractions of coarse secondary phase particles.

Steel	Coarse secondary phase particles/inclusions based on SEM-EDS (+oxides and oxysulfides)	Calculated area fractions (%)		
		A_{c3}+60 s	A_{c3}+180 s	Total (avg.)
Ref	MnS; TiN; Al_2O_3+TiN, Ti(C,N)	0.094	0.065	0.080
A	MnS; Al_2O_3; TiN; Al_2O_3+TiN; $Ti_4C_2S_2$; TiC; Ti(C,N)	0.172	0.169	0.171
B	MnS; Al_2O_3; TiN; (Ti,V)N, Al_2O_3+(Ti,V)N; (Ti, Vn)(C,N)	0.068	0.080	0.074
C	MnS; Al_2O_3; TiN; TiN+Al_2O_3;	0.087	0.082	0.085
D	MnS; Al_2O_3; TiN, (Ti,V)N; Al_2O_3+(Ti,V)N; (V,Ti,Mo)C; (V,Ti,Mo)(C,N)	0.080	0.093	0.087
E	MnS; Al_2O_3	0.061	0.064	0.063

In addition to the particle/inclusion types listed in Table 4, the EDS analysis indicated that a small amount of oxysulfides were present in all steels. Steel A, alloyed with a hyperstoichiometric amount of Ti (0.09 %), contained the highest amount of coarse secondary phase particles, whereas the measured amounts were smallest in Steel E. Regarding the nature of the characterization process, the determined particle fractions of Steels B, C, D, and E are at the same level. Steel E contained the smallest amount of particles due to intentional absence of Ti and Al, both of which are nitride formers. The largest particle area fraction of Steel A must be related to the presence of a relatively large amount of $Ti_4C_2S_2$ that has been reported for example in [40-42]. In the case of laboratory steels, no clear differences were identified between the examined austenitization times of A_{c3}+60 s and A_{c3}+180 s. However, industrially manufactured reference steel Ref, showed larger scatter between the austenitization times (Table 4). In Ref, relatively coarse pure TiN were present (Fig. 7a). Regarding the slightly higher Ti content of Ref (Table 1), the area fraction of TiN was most likely higher than in Steels A-D, but on the basis of our analysis, the fraction of aluminium oxides (Al_2O_3) was clearly smaller. It can be evaluated that due to this reason the aggregate amount of coarse particles was comparable between Ref and laboratory Steels A-D.

3.5. Nano-sized carbide and carbo-nitride precipitates

The combination of alloying elements and processing history determines the size and density of precipitates in the micro alloyed Steels A, B, C, and D. Regarding the hot rolling histories of the laboratory steels, precipitation of Ti and V containing particles may have started already during hot rolling as a strain induced precipitation [27]. However, according to current understanding [27] both TiC and V(C,N) have pronounced avidity to precipitate at lower temperatures starting approximately from 650 ˚C (923 K), in conjunction with a slow cooling rate and austenite decomposition. The precipitation mechanisms are not, however, addressed further in the present study, but the precipitation characteristics will be discussed in a general level in order to explain their roles in mechanical behavior. In contrast to micro alloyed hot-rolled steels, press hardening steels are additionally subjected to cold-rolling, and reaustenitization cycles (~900 ˚C (1173 K)) prior to die-quenching. Therefore, the precipitate structures may change significantly as a result of the subsequent heat treatments. In particular, the role of austenitization parameters of the press hardening process needs to be carefully considered. Fig. 7 and 8 present the summarized results of the TEM analysis.

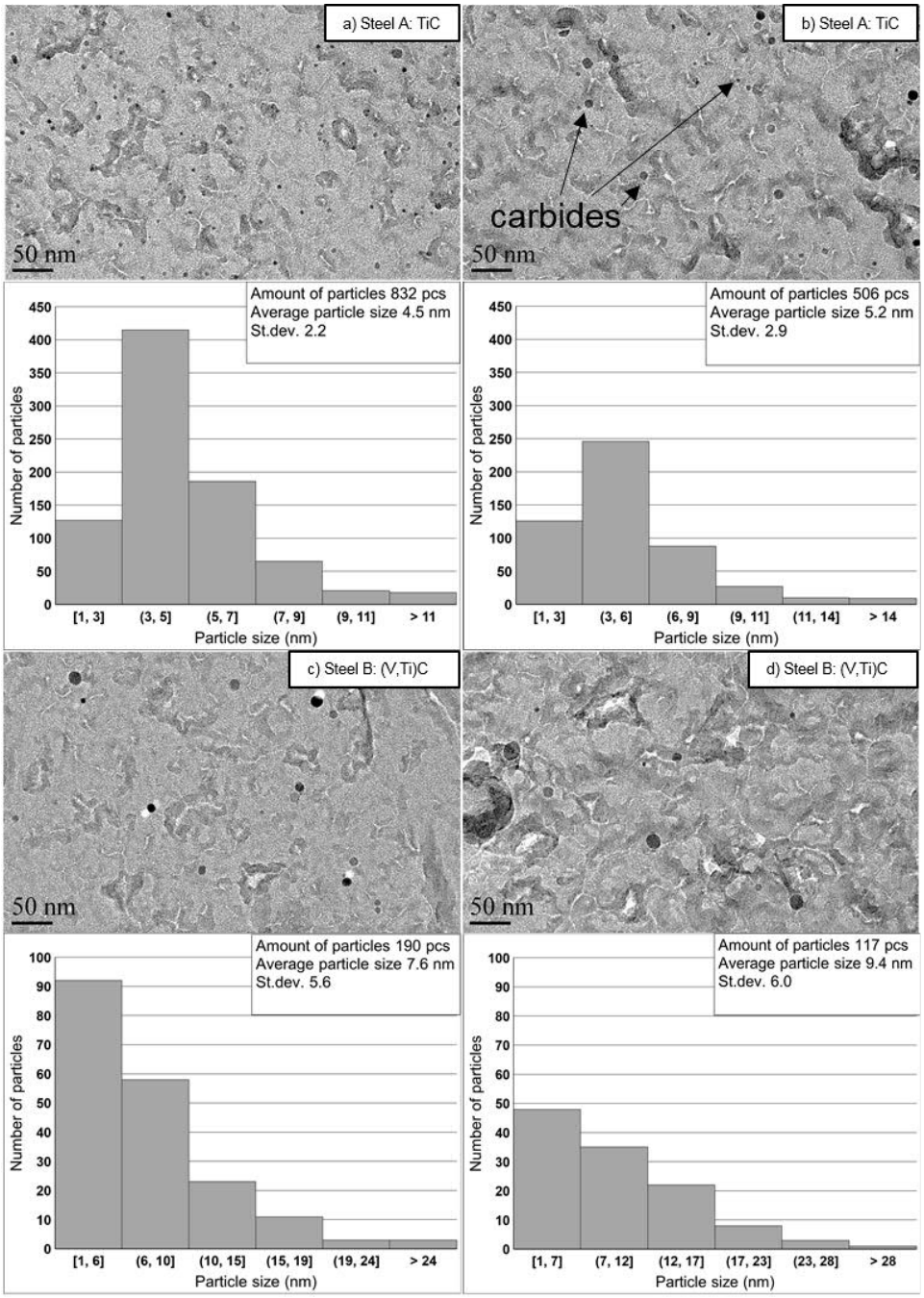

391

392 **Fig. 7.** Results of TEM-analysis (carbon extraction replicas) for the Cr alloyed steels. Steel A in the PH

393 condition after austenitizing for; a) A_{c3}+60 s; b) A_{c3}+180 s at 900 ˚C (1173 K). Respectively, results of

394 Steel B after austenitizing for; c) A_{c3}+60 s; d) A_{c3}+180 s.

395

As indicated in Fig. 7a and 7b, a large amount of fine TiC precipitates are present in the samples of Steel A after both austenitization cycles. This implies that high amount of Ti has been available for precipitation. In other words, almost all Ti except to extremely stable TiN and $Ti_4C_2S_2$ must have dissoluted during the reannealing carried out at 1250 ˚C (1523 K) for 1 h [40]. The longer austenitization time of A_{c3}+180 s (Fig. 7b) has not markedly increased the average precipitate size (from 4.5 nm to 5.2 nm), but has decreased the frequency of precipitates (from 832 to 506) and increased scatter in the precipitate size. Accordingly, a small scale coarsening of Ti containing precipitates has occurred between the examined austenitization cycles. The attained results are in line with the PAGS measurements (section 3.3): the comparison of the PAGB maps (Fig. 5a and 5c) suggests that the decrease in the amount of stable precipitates has led to a moderate increase in the PAGS. However, the stability of TiC is known as relatively good as discussed for example in [43]. This explains the presence of large amount of fine 1-10 nm precipitates even after the longer austenitization cycle of A_{c3}+180 s/900 ˚C (1173 K). In addition, it is well known [27] that the carbides and nitrides of Ti and V are B1 NaCl (Fm3m) by their structure. Regarding this, it is not reasonable to analyze the structure of individual precipitates more in detail in the present study.

Fig. 7c and 7d show the results of the TEM analysis for Steel B. According to the TEM-EDS analysis, mixture carbides of (V,Ti)C were mainly present. By comparison, the amount of V based carbides in Steel B is clearly smaller than the amount of TiC observed in Steel A. In addition, the precipitate size is clearly larger in Steel B and the precipitate size has increased stronger with the prolonged austenitization time. Based on this, the prolonged soaking at the furnace temperature of 900 ˚C leads to the coarsening and dissolution of V containing precipitates. This theory is supported by the PAGS measurements (Table 3), since the PAGS of Steel B are larger compared to Steel A. Nevertheless, there are still a relatively large amount of precipitates remaining even after the longer austenitization cycle of A_{c3}+180 s. To

elucidate the differences in the attained precipitate structures, the theory of V micro alloying needs to be briefly considered. As noted for example in [28; 44], V has much higher solubility in austenite compared to Ti, and thus complete dissolution at 1250 ˚C (1523 K) can be expected even with the present contents of around 0.15 % V and 0.35 % C which are relatively high [28]. This means that a large amount of V has been free for precipitation. The precipitation of more stable VN could have also occurred, but is believed to be insignificant in Steel B, since both Ti and Al have higher affinity for N and should have combined to form (Ti,Al)N [43]. As indicated in Table 3, some V was present in coarse precipitates of (Ti,V)N and (Ti,Vn)(C,N). From the dispersion hardening point of view, the precipitation of VC is preferred in V containing steels [28]. This theory is also supported by the present results showing only V rich carbides in the carbon extraction replicas of Steel B (Fig. 7c and 7d).

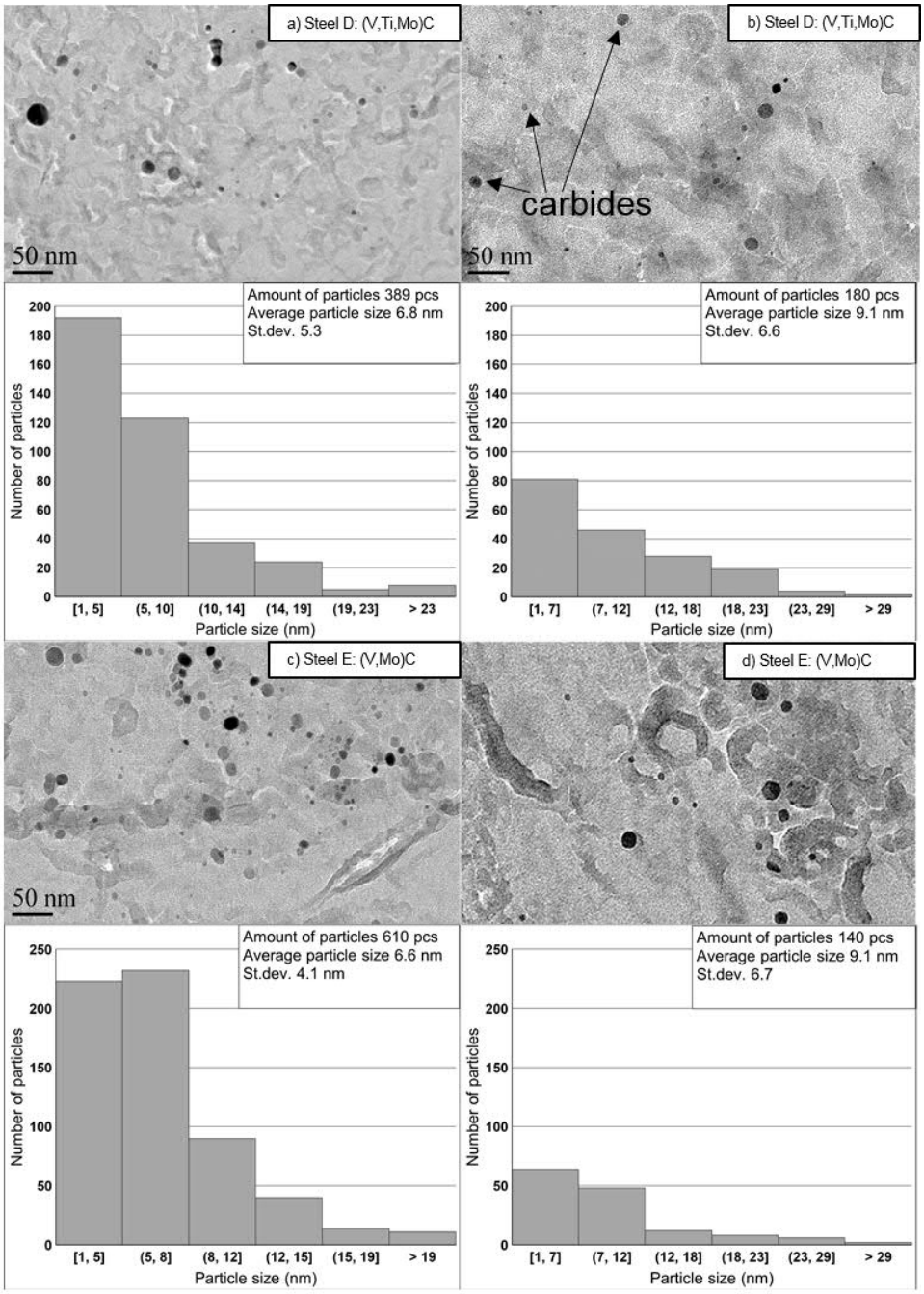

Fig. 8. Results of TEM-analysis (carbon extraction replicas) for Mo alloyed steels: Steel D in the PH condition after austenitizing for a) A_{c3}+60 s; b) A_{c3}+180 s at 900 ˚C (1173 K). Respectively, results of Steel E after austenitizing for; c) A_{c3}+60 s; d) A_{c3}+180 s.

436 The TEM analysis carried out for Steel D (Fig. 8a and 8b) showed larger amount of V based carbides
437 compared to Steel B (Fig 7c and 7d). In the case of Steel D, a majority of the carbides were identified as
438 mixture carbides of (V,Ti,Mo)C. Similarly to Steel B, the longer austenitization time (Fig. 8b) decreased
439 the amount of precipitates and increased also the precipitate size. However, the coarsening of V
440 containing mixture carbides (V,Ti,Mo)C was slightly smaller in Steel D, which is also supported by
441 slightly smaller PAGS in Steel D (Table 3). The effects of Mo alloying are in line with the literature: it
442 has been reported that Mo can improve the thermal stability of Ti containing precipitates [45], and thus
443 same effects can be expected here in the case of VC. Furthermore, Mo decreases the austenite
444 decomposition temperature by favoring bainite formation instead of pearlite [23]. Hence, precipitation
445 process, occurring mainly during the austenite decomposition, starts generally at lower temperatures
446 which can also refine the average precipitate size [46].
447
448 As indicated in Fig. 8c and 8d, Steel E exhibited the most interesting precipitate structures: the amount
449 of (V,Mo)C is notably high in the sample that was austenitized for A_{c3}+60 s/900 ˚C (1173 K) (Fig. 8c),
450 but the prolonged austenitization time of A_{c3}+180 s/900 ˚C (1173 K) decreased the amount precipitates
451 drastically (Fig. 8d). The trend of precipitate coarsening can be also clearly seen in the form of larger
452 PAGS results (Table 3). Considering the precipitate structures of V containing steels after A_{c3}+60 s, the
453 amount of middle size precipitates (5-12 nm) is clearly highest in Steel E. However, the average
454 precipitate sizes are comparable with Steel D and slightly smaller than in Steel B. The attained
455 precipitate sizes could be at least partially explained with stability differences between V containing
456 carbides. Accordingly, the mixture carbides of (V,Mo)C formed in Steel E and (V,Ti)C formed in Steel
457 B, have coarsened more than the most complex (V,Mo,Ti)C observed mainly in Steel D. Exceptionally
458 large amount of V containing precipitates in Steel E (Fig. 8a) suggests that the precipitation has occurred
459 within a wide range of temperatures. In addition, the contribution of nitrogen and successive formation

of V(C,N) must be considered here, since Steel E did not practically contain other nitride forming elements Ti, Al, and B. However, TEM-EDS analysis did not reveal the presence of N either in the V containing precipitates, and thus the attained results do not fully explain the observed behavior. Despite this, there are reasons to believe that large amount of N containing precipitates are actually present in Steel E, and it is possible that there has been difficulties to identify N with EDS. As noted by Lagneborg et al. [44] the precipitation of V containing precipitates starts with N rich V(C,N). After that, the precipitation of V(C,N) propagates with constantly increasing C content and occurs finally as pure VC. Therefore, it is believed that the precipitation N rich V(C,N) should have occurred in the early stages of the precipitation process. However, the employed carbon extraction replica technique has not been appropriate for revealing the presence of those precipitates.

3.6. Tensile behavior

Tensile testing at a quasistatic strain-rate of 5 x $10^{-4}s^{-1}$ was carried out for the specimens in both PH and PH+BH conditions. Fig. 9 presents example engineering stress-strain curves for Steel D in both PH and PH+BH conditions.

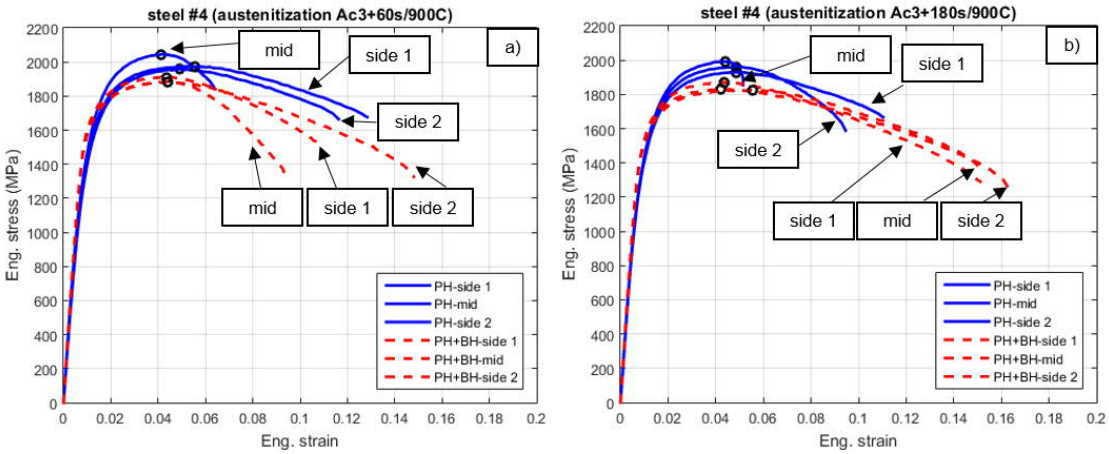

Fig. 9. Tensile test curves for Steel D in the case of both austenitization cycles of; a) A_{c3}+60 s; b) A_{c3}+180 s at 900 ˚C (1173 K). The curves measured in both press-hardened (PH) and additionally bake

hardened (PH+BH) conditions are presented. The peaks of the curves indicating uniform elongation and ultimate tensile strenght are marked using black circles.

The presented stress *vs.* strain curves (Fig. 9) represent the behavior of three parallel specimens. The observed tensile behavior followed the same trend in the case of all steels: the specimens that were cut from the middle part of the sheets showed highest strength, but lowest total elongation values. The other two specimens were cut closer to the edges of the sheet. Those specimens exhibited slightly smaller strength values but larger total elongation. This behavior must have been caused by local cooling rate differences in the die-quenched samples, indicating that the highest cooling rate and surface pressure was achieved in the middle parts of each sheet sample. Regarding this, the auto-tempering of martensite has been more significant in the specimens cut from the side areas. The scatter between the side specimens is most likely natural by nature. It is however believed that the averaged values from three parallel tests correlate well with the properties of industrially produced components, which are also involved with local cooling rate differences. The mechanical properties are summarized in Table 5.

Table 5. Mechanical properties for the investigated steels in both PH and PH+BH conditions. Post-uniform elongation values are only used for the comparison between the investigated steels.

	A_{c3}+60 s/900 °C (1173 K) - PH					A_{c3}+60 s/900 °C (1173 K) - PH+BH				
Steel	**$R_{p0.2}$ (MPa)**	**R_m (MPa)**	**$R_{p0.2}/R_m$**	**A_g (%)**	**Post-uniform elongation (%)**	**$R_{p0.2}$ (MPa)**	**R_m (MPa)**	**$R_{p0.2}/R_m$**	**A_g (%)**	**Post-uniform elongation (%)**
Ref	1480	2120	0.70	5.4	2.0	1620	1960	0.83	4.8	7.2
A	1370	2000	0.69	5.1	2.6	1530	1850	0.83	4.1	5.3
B	1350	1990	0.68	5.2	4.7	1500	1860	0.81	4.7	9.5
C	1320	1980	0.67	5.3	5.4	1510	1870	0.81	4.4	7.1
D	1360	1990	0.68	4.9	5.5	1560	1890	0.83	4.4	7.4
E	1340	1980	0.68	4.6	1.4	1640	1960	0.84	4.5	7.2

	A_{c3}+180 s/900 °C (1173 K) - PH					A_{c3}+180 s/900 °C (1173 K) - PH+BH				
Steel	**$R_{p0.2}$ (MPa)**	**R_m (MPa)**	**$R_{p0.2}/R_m$**	**A_g (%)**	**Post-uniform elongation (%)**	**$R_{p0.2}$ (MPa)**	**R_m (MPa)**	**$R_{p0.2}/R_m$**	**A_g (%)**	**Post-uniform elongation (%)**
Ref	1460	2120	0.69	5.4	2.6	1550	1950	0.79	4.8	7.2
A	1320	1950	0.68	4.3	2.6	1490	1840	0.81	4.3	7.5
B	1300	1940	0.67	4.4	4.7	1440	1840	0.78	4.9	8.3
C	1290	1940	0.67	4.8	4.6	1430	1810	0.79	4.3	7.7
D	1330	1960	0.68	4.7	3.9	1480	1840	0.80	4.7	10.9
E	1300	1910	0.68	3.7	2.3	1470	1850	0.79	4.2	6.2

In principle, the measured strength values of Steels A-D (Table 5) are typical for martensitic steels having C contents of 0.34-0.35 %, but for some reason, the values are systematically lower compared to the industrially manufactured reference steel Ref. The higher strength of the Ref could be at least partially explained by the smaller sheet thickness of 1.1 mm, which naturally leads to the higher cooling rate in die-quenching. This should hinder the auto-tempering behavior and result in the formation of harder martensite. This interpretation is in line with the results reported by Tabata et al. [47]. The scientists showed that higher cooling rate below M_s correlated with higher yield and tensile strength in 22MnB5 steels. In the present case, the $R_{p0.2}$ values of Ref (1480 MPa and 1460 MPa) are higher than the values measured for a micro alloyed 34MnB5 grade (1.5 mm), i.e., 1430 MPa and 1410 MPa studied in our previous study [11]. Therefore, it is believed that in particular the yield strength of Ref is affected by higher cooling rate below M_s that has hindered the auto-tempering of Ref. To take another view, it is also possible that industrially produced grades contain lower level of oxides. This factor was actually observed during the analysis of the coarse secondary phase particles (section 3.4).

3.7. 3-point bendability

3-point bending tests (VDA 100-238) were carried out for the PH and PH+BH samples austenitized for A_{c3}+180 s at 900 ˚C (1173 K). Figure 10 presents averaged values for maximum bending angle at maximum bending force α_{Fmax} along with representative load vs. displacement curves.

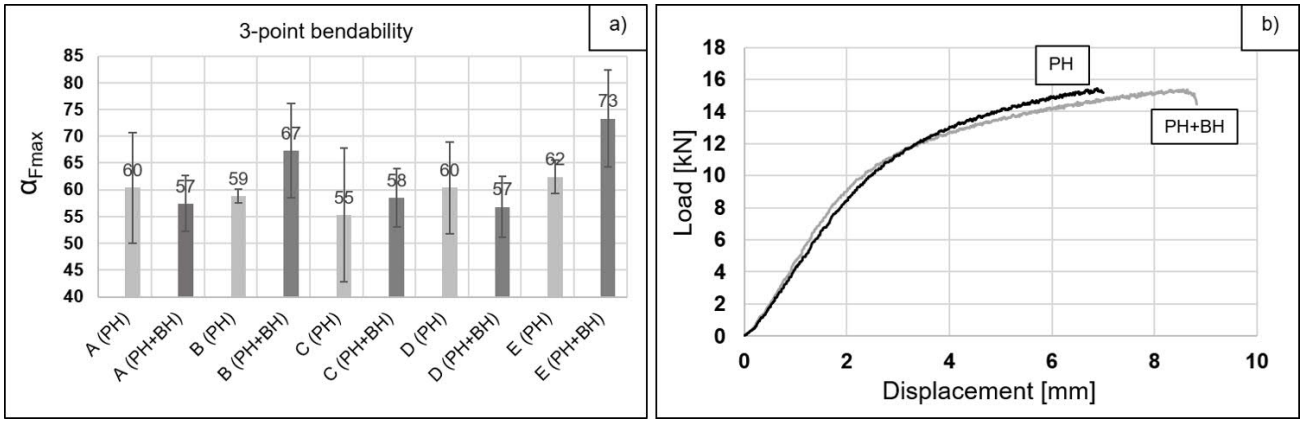

Fig. 10. a) Results of 3-point bending tests expressed as maximum bending angle at maximum force (α_{Fmax}) for the laboratory Steels A-E in both PH and PH+BH conditions. b) Examples of load vs. displacement curves.

The attained α_{Fmax} values imply that all steels showed almost comparable bending behavior, i.e., α_{Fmax} values of 55-62˚ when tested in the PH condition. Correspondingly, the values measured in PH+BH condition were 57-73˚ with larger scatter between the studied steels. Based on the present results, the positive effect of the BH treatment is not as unambiguous as observed according to the tensile test results (Table 5). Steels B and Steels E showed clear increase of 8-9˚, whereas Steels A and D exhibited small decrease in α_{Fmax} as a result of the BH treatment. Steel A, in turn, showed only a small increase of 3˚. However, as illustrated in Fig. 10a, the scatter between parallel tests was relatively large. Therefore, it is difficult to evaluate if the obtained trends in α_{Fmax} are real or just caused by large scatter of the test method. In particular, the measured decreases after the BH treatment, i.e., Steels A and D are qustionable. All in all, the measured bending angles (Fig. 10a) are at a relatively good level regarding

533 the C content (0.34-0.35 %) and strenght level (~1900 MPa). By comparison, typical bending angle for
534 22MnB5 with PAGS of around 20 μm has been reported to be 55-60 ˚ [8].
535
536 **4. Discussion**
537
538 **4.1. Relationships between microstructures and strength**
539
540 Based on the current understanding [48], the PAGS correlates well with the packet and block size of
541 martensite, and can be thus used to evaluate the desired grain refinement in martensitic PHS. The
542 present results (Table 3) indicate that very fine PAGS of 2-6 μm can be attained when micro alloying
543 with Ti or V, since the values are generally smaller compared to Ref. Thus, substantial grain size
544 refinement was achieved with the alloying concepts of the present study. By comparison, the PAGS
545 determined for several 22MnB5 grades in [31] were 5-8 μm after austenitizing for 180 s at 900 ˚C (1173
546 K). The PAGS of the present study are smaller, i.e., 2-4 μm after austenitizing for approximately 180 s
547 at 900 ˚C (1173 K), even though there is larger driving force for the grain growth in 34MnB5 grades
548 compared to 22MnB5.
549
550 It is widely accepted that C content is the most dominating factor determining the strength of martensitic
551 steels [3]. Some previous studies [6, 17, 49] have reported on the improved strength values due to micro
552 alloying. However, practically attainable strength increment provided by micro alloy precipitates is not
553 currently clear in 34MnB5 based steels. Fig. 11 depicts the correlation between PAGS and strength
554 values for the investigated steels in the PH condition.
555

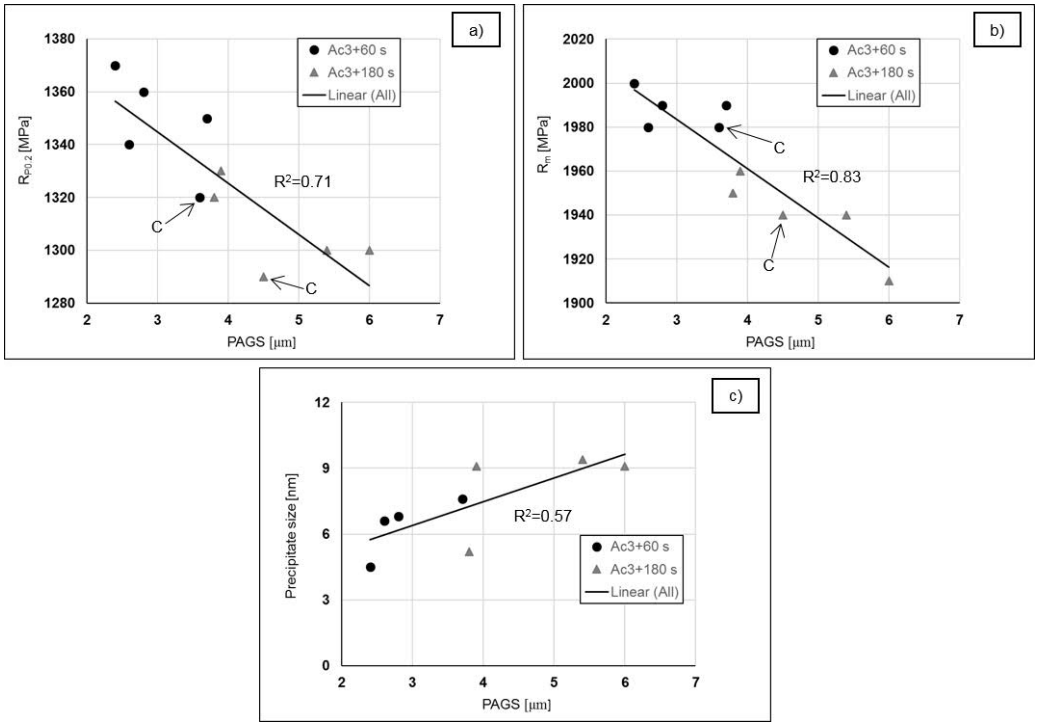

Fig. 11. a) Correlation between yield strength ($R_{p0.2}$) and prior austenite grain size (PAGS). b) Correlation between tensile strength (R_m) and PAGS. c) Correlation between precipitate size (micro alloyed Steels A, B, D, and E) and PAGS. Results of Ref are omitted due to smaller sheet thickness.

The trends and values presented in Fig. 11 suggest that the strength of martensitic 34MnB5 steels can be increased some tens of MPa through the practically achievable PAGS refinement. The attained strength values are consistent with earlier studies [31, 50], which have also shown the linear relationships between PAGS and strength of martensite. However, on the basis of the absolute values, micro alloying or industrially attainable grain size refinement cannot provide substantial effect on the strength of martensitic steels in the PH condition.

In addition, Fig. 11 indicates that PAGS refinement and slightly increased strength are attributed to the micro alloying with V and Ti. To clarify, Steel C (no micro alloying) showed the smallest $R_{p0.2}$ values with both austenitization times. However, a closer look into graphs in Fig. 11a and 11b reveals that also

other factors need to be pointed out. The measured PAGS of the Steel C, alloyed with 0.30 % Mo, were slightly smaller than the PAGS of Steel B, alloyed with a combination of 0.30 % Cr + 0.15 % V. This result suggests that micro alloying does not necessarily result in smaller PAGS in 34MnB5 type steels. To explain this discrepancy, the initial microstructures of Steels B and C need to be taken into account. As presented in Fig. 1, the microstructure of Steel C is clearly finer and more uniform with respect to cementite distribution. Our earlier study [31] showed that the initial microstructure of 22MnB5 steel has a clear effect on the PAGS. In that study finer and more uniform distribution of pearlite/cementite resulted in the most efficient refinement of the PAGS, whereas the typical cold-rolled microstructure (full-hard) of 22MnB5 consisting of large pearlite colonies and slightly elongated ferrite grains, resulted in the larger PAGS and slightly smaller strength values. Hence, it is believed that the differences in the initial microstructures are responsible for the observed behavior between Steels B and C. Regarding this, an appropriate control of the initial microstructure can compensate the absence of micro alloying elements at a relatively low austenitization temperatures of around 900 ˚C (1173 K). The importance of the initial microstructure has been also addressed in [18] and [51].

Fig. 11c shows that there is correlation between precipitate size and PAGS, and thus supports the conclusion that the presence of micro alloy precipitates have a significant role in the PAGS refinement. In the present study, the average precipitate size was approximately 6-10 nm in V micro alloyed Steels B, D, and E, which is generally larger than the size of TiC precipitates in Steel A, i.e., around 5 nm (Fig. 7 and 8). Slightly smaller PAGS of Steel A (Table 3) are in line with the study of Matsumoto et al. [21]. They reported that Ti is more effective than V when it comes to grain refining effect, because rapid dissolution of VC occurs above 900 ˚C (1173 K). This is supported by the TEM analysis (Fig. 7 and 8), however, it seems that the presence of Mo and Ti can hinder the coarsening of VC as already discussed in section 3.5.

4.2. Effect of micro alloying concept on the bake hardening behavior

The simulated BH treatment of 170 ˚C (423 K)/20 min had a strong influence on the mechanical properties of 34MnB5 steels (Table 5). Fig. 12a and 12b illustrate the relationships between PAGS and attained changes in strength values expressed in terms of $\Delta R_{p0.2}$ (increase in yield strength) and $-\Delta R_m$ (decrease in tensile strength). Fig. 12c, in turn, connects the measured precipitate size with $\Delta R_{p0.2}$.

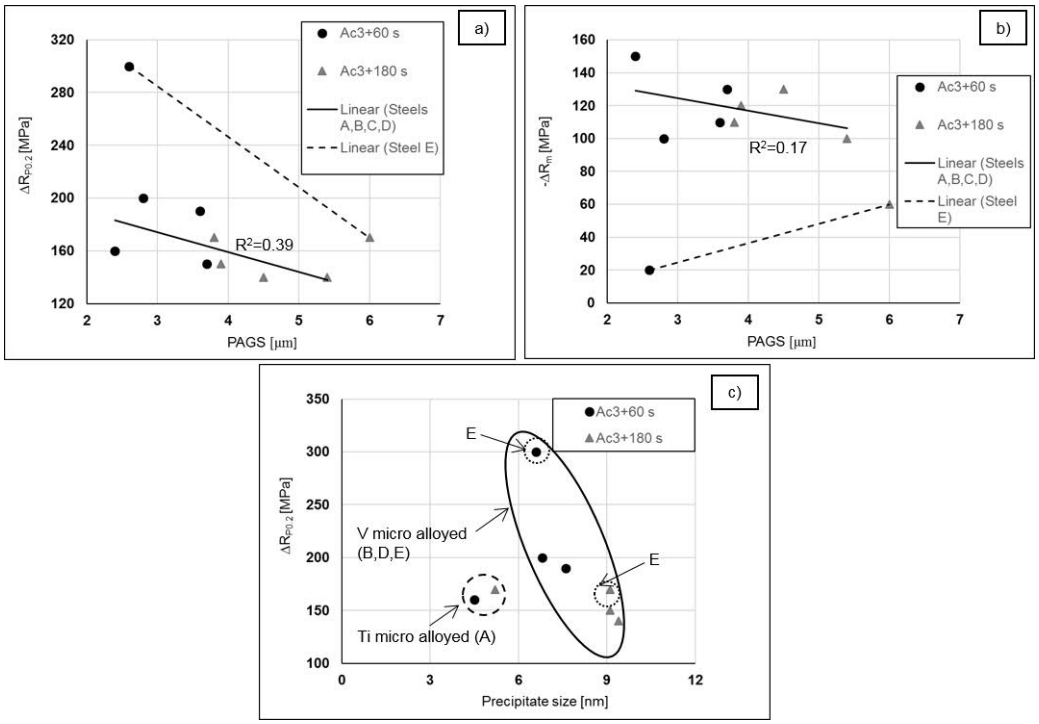

Fig. 12. a) Correlation between the attained increase in yield strength ($\Delta R_{p0.2}$) and parent austenite grain size (PAGS) after the bake hardening (BH) treatment. b) Correlation between the attained decrease in tensile strength ($-\Delta R_m$) and PAGS, respectively. c) Correlation between $\Delta R_{p0.2}$ and precipitate size. The graph shown in b) presents only the results of micro alloyed Steels A, B, D, and E. Results of Ref are omitted due to smaller sheet thickness.

609 Fig. 12a suggests that the finer PAGS correlates generally with the larger $\Delta R_{p0.2}$, even though the
610 attained correlation is not strong. Still, a corresponding trend was observed for conventional 22MnB5
611 steels in our earlier study [11]. Based on the widely accepted literature [38, 52] and conclusions made in
612 [11], the attained increase in $R_{p0.2}$ is understood to be connected with the formation (or increased
613 amount) of fine Fe based carbides, i.e., transition carbides and fine cementite precipitates, and their
614 interactions with existing dislocations. This theory is supported by the present SEM analysis (Fig. 2)
615 suggesting that the amount of fine cementite is increased in the BH treatment. Based on this, the
616 formation of fine Fe based precipitates has an important role in the mechanical behavior, since they
617 shorten the mean free path of dislocation glide. Accordingly, the smaller PAGS should result in more
618 difficult dislocation motion, since smaller PAGS increases the dislocation density of martensite [53].
619 The attained results of V micro alloyed Steels B, D, and E are consistent with this theory: finer PAGS
620 and smaller precipitate size correlated clearly with larger $\Delta R_{p0.2}$ (Fig. 12a). The results of Ti alloyed
621 steels are, however, contradictory. Steel A showed the smallest PAGS (Table 3) together with the largest
622 amount of nano-sized precipitates (Fig. 7). Despite this, the $\Delta R_{p0.2}$ values of Steel A were not the highest
623 of all. As indicated in Fig. 12c the $\Delta R_{p0.2}$ values did not either show corresponding correlation with
624 precipitate size as in the case of V micro alloyed steel, since no significant coarsening of TiC
625 precipitates was observed due to higher stability of TiC. Nevertheless, an increase in the PAGS from 2.4
626 to 3.8 μm was measured, which should promote dislocation glide and smaller $R_{p0.2}$ after the longer
627 austenitization cycle. Hence, more investigations would be needed to understand this discrepancy.
628
629 In fact, the results of Ti micro alloyed Steel A are very similar to our previously published results on Nb
630 micro alloyed 34MnB5 steel addressed in [11]. In that study, no clear correlation between increased
631 PAGS (from 4.6 μm to 7.6 μm) and BH induced increase in $R_{p0.2}$ was found: the values were around 150
632 MPa in the case of short (~3 min) and long (~7.5 min) austenitization times at 900 ˚C (1173 K). The

633 possible factors have been discussed more in detail in [11] and will not be addressed in the present
634 study. It can be only evaluated that the different behavior between Ti (or Nb) and V micro alloyed steels
635 may be attributed to the characteristic misfit values between micro alloy precipitates and matrix. As
636 described by Baker [27], the V(C,N) precipitates are an exception and can retain their coherency with a
637 much higher size in comparison with TiC and NbC [27]. Hence, coherent Ti or Nb based precipitates are
638 not practically present in Ti and Nb micro alloyed steels. It is generally understood [54] that coherent
639 needle-like precipitates are cut by dislocations, and thus the strengthening mechanism (increase in yield
640 strength) is stronger than provided by incoherent spherical precipitates, which more preferably result in
641 the bowing of the dislocation fields. Therefore, a relatively large $\Delta R_{p0.2}$ values in V containing Steels B,
642 D, and E may be also attributed to the interactions between existing dislocations of martensite and fine
643 coherent V based precipitates, in conjunction with incoherent spherical precipitates that were observed
644 in the TEM analysis (Fig. 7 and 8). The shorter austenitization time promotes retaining the coherency of
645 precipitates. In the present study, the longer austenitization cycle decreased the $\Delta R_{p0.2}$ values of V micro
646 alloyed steels, which may be connected with the loss in coherency. However, this behavior is most likely
647 also associated with the increase in PAGS (Table 3), since larger grain size decreases dislocation density
648 as discussed above.
649
650 The graphs presented in Fig. 12a and 12c reveal that Steel E exhibited a distinctive mechanical behavior
651 in the PH+BH condition: there are exceptionally large differences in the measured $\Delta R_{p0.2}$ values between
652 the investigated austenitization cycles of A_{c3}+60 s/900 ˚C (1173 K) and A_{c3}+180 s/900 ˚C (1173 K). The
653 difference itself could be explained with the remarkable decrease in the density of nano-sized V
654 containing precipitates (Fig. 8c and 8d). However, the $\Delta R_{p0.2}$ value of 300 MPa is extremely high. Based
655 on previous research works and understanding on the strengthening mechanisms of V micro alloyed
656 steels [44, 46], the observed behavior can be only explained with the presence of relatively large amount

of V(C,N). Kostryzhev et al. [54] have reported that the strengthening mechanisms provided by coherent and incoherent precipitates are different. Hence, is it believed that the precipitation hardening provided by fine and coherent V(C,N) precipitates can compensate the tempering of martensitic matrix, which tends to significantly decrease the tensile strength of 34MnB5 based steels. This is in line with the fact that a decrease of only 20 MPa was measured in Steel E. The present study cannot provide evidence on the presence of coherent V(C,N) precipitates, but Hutchinson et al. [20] reported similar type of results for V-N micro alloyed martensitic steels. In that study martensitic steels were tempered at higher temperatures and V-N alloyed steels showed highest tempering resistance. Either Hutchinson et al. [20] were not able to identify coherent V containing precipitates with TEM, and thus their conclusion was partially speculative. However, they observed the presence of V clusters in matrix with TEM-EDS and suggested that the mechanism behind tempering resistance is most likely the formation of coherent VN precipitates that are extremely difficult to identify even from TEM foil samples.

4.3. Relationships between microstructural features and ductility

While fine nano-sized precipitates are generally considered valuable, the detrimental role of coarse secondary phase particles has been discussed in recent research works. For example, Bian and Mohrbacher [16] suggested discarding the traditional concept of Ti-B alloying by arguing that hard and coarse TiN particles decrease resistance to crack initiation: the particles act as sites for void formation during tensile testing and 3-point bending. Therefore, it is meaningful to pay attention to the role of secondary phase particles. Fig. 13 presents the relationship between the measured amount of coarse secondary phase particles and post-uniform elongation in both PH and PH+BH conditions.

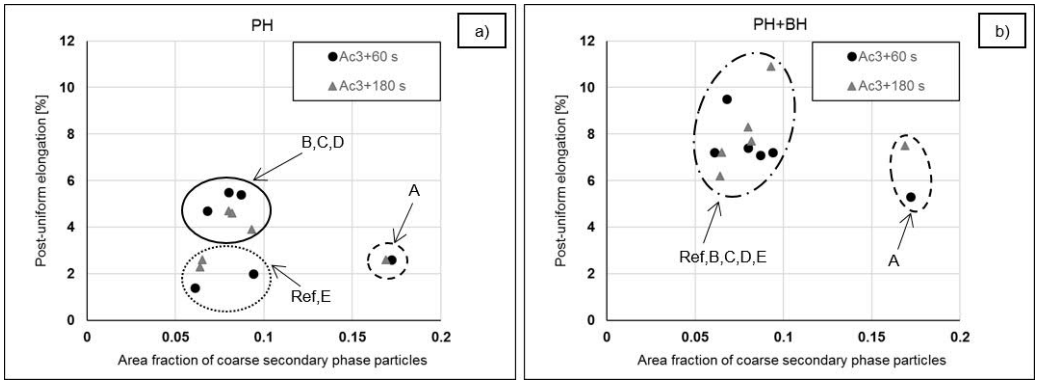

Fig. 13. Correlation between the area fraction of coarse secondary phase particles and post-uniform elongation in; a) press-hardened (PH) condition; b) press-hardened and additionally bake hardened (PH+BH) condition.

As indicated in Fig. 13a, the presented data may be divided into three distinct groups. The first group, consisting of Steels B, C, and D, combines moderate amount of secondary particles and relatively large post-uniform elongation values of around 4-6 %. The results of Steel A form the second group by combing a limited post-uniform elongation of around 2-3 % and the highest area fraction of coarse secondary phase particles. The correlation between poor ductility and large amount of inclusions is reasonable, whereas the correlation between elongation and very fine PAGS is not expected (Table 3). The third group comprises the results of two steels, i.e., Ref and Steel E. These steels showed even slightly smaller post-uniform elongation of 2 % despite the small amount of inclusions. In particular, the results of Steel E are confusing regarding the fine PAGS (2.6 μm) attained after short austenitizing cycle of A_{c3}+60 s. It can suggested that the behavior of Ref is dominated by the presence of largest amount of hard untempered martensite, since the smaller sheet thickness of 1.1 mm must have increased the cooling rate and hindered the auto-tempering. This idea is consistent with the findings of Leslie and Sober [55], who reported that the mechanical behavior of martensite is more and more dominated by strong dislocation locking when C contents above 0.30 % are present. The proposed theory underlines the important role of C content, whereas the cooling rate effects has been discussed previously in [47]

700 and [18]. Regarding the largest total amount of precipitates in Steel A, i.e., the sum of nano-sized
701 precipitates (Fig. 7) and coarse precipitates (Table 3), the limited post-uniform elongation values are
702 explainable. However, as discussed in section 4.2, it is believed that the incoherent spherical precipitates
703 do not interact with existing dislocations as strongly as coherent precipitates. This theory could explain
704 the very limited plasticity of Steel E which is contradictory with the smallest amount of coarse
705 inclusions.
706
707 The presented tensile test result (Table 5) showed consistently improved ductility due to the simulated
708 BH treatment. As illustrated in Fig. 13b, the BH treatment equalized the mutual differences between
709 Steels B, C, and D, E, and Ref. This indicates that the increased plasticity of martensite, i.e., tempering
710 of martensitic matrix, correlates strongly with the improved post-uniform elongation in the steels of
711 34MnB5 type. In addition, it seems evident that the increased plasticity of BH treated martensite can
712 greatly compensate the ductility loss caused by the precipitation hardening from coherent precipitates
713 (Steel E) or by the presence of large amount of secondary phase particles (Steel A).
714
715 **4.4. Relationships between microstructural features and 3-point bendability**
716
717 Larour et al. [7] suggested that post-uniform properties correlates best with 3-point bendability and crash
718 behavior, but the positive relationships is difficult to demonstrate with standard tensile specimens. This
719 is because post-uniform elongation is highly underestimated in conventional tensile tests and total
720 elongation, i.e., fracture elongation, depends strongly on the specimen gauge length. In the present
721 study, the small gauge length of 8.0 mm may have enhanced the possibility or more reliably assessment
722 of the local ductility. Nevertheless, additional 3-point bending tests were involved in the present study to
723 tackle the above mentioned challenges. Fig. 14a presents the correlation between post-uniform

elongation and maximum bending angle at maximum force (α_{Fmax}). In addition, 3-point bending results of correspondingly heat-treated (A_{c3}+180s/900 ˚C (1173 K)) ZnFe coated 22MnB5 are presented for comparison in Fig. 14b.

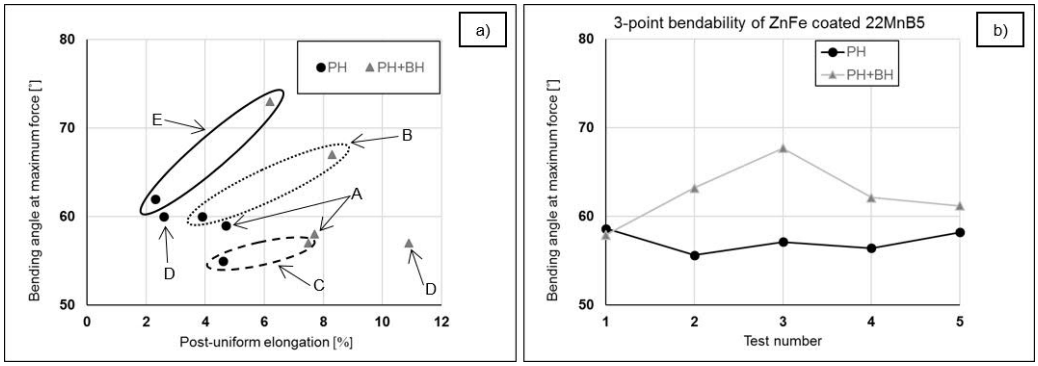

Fig. 14. a) Correlation between post-uniform elongation and 3-point bendability for PH and PH+BH treated laboratory Steels A-E. b) 3-point bending data (5 parallel tests) for a reference grade, ZnFe coated 22MnB5 in both PH and PH+BH conditions after corresponding austenitizing cycle of A_{c3}+180 s at 900 ˚C (1173 K).

Fig. 14a shows that the expected correlation between post-uniform elongation and 3-point bendability (Fig. 10a) was observed for certain steels, i.e., Steels B, C and E showed improved α_{Fmax} values as a fucntion of larger post-uniform elongation. This positive trend is supported by the results of Dietchs et al. [12]. They reported bending angle improvements from 44˚ to 51˚ as a result of the BH treatment in the case of AlSi coated PHS (tensile strenght around 1900 MPa). Therefore, the present results of Steels B, C, and D are reasonable and can be explained with the decreased dislocation density of martensite occurring during LTT treatments [53] and increased amount of slip systems [39, 56]. However, when the same data (Fig. 14a) is reviewed as individual groups of PH and PH+BH treated samples, a negative correlation between post-uniform elongation and α_{Fmax} can be seen. This trend is totally unexpected and is most likely caused by other microstructural features. Choi et al. [15] pointed out that the decarburization layer with soft ferritic microstructure improves significantly the bendability of 22MnB5

steel, while it does not have substantial effect on the tensile properties. Therefore, it is believed that the differences in the sub-surface microstructures (Fig. 3) are responsible for the high scatter seen in 3-point bending results and greatly complicates the comparison of steels with different chemical compositions.

In addition to microstructures, a relatively large scatter in the bending test results (Fig. 10a) needs to be noted. In order to assess the role of natural scatter, a ZnFe coated 22MnB5 steel was chosen as a reference (Fig. 14b): the coating prevents decarburization of the surface, and thus allows more reliable comparison between parallel tests. The data shows surprisingly small scatter between individual tests and suggests that the relatively large scatter seen in Fig. 10a, must be mainly caused be other factors outside the natural scatter. Furthermore, the positive effect of the BH treatment, i.e., the improvement of about 5˚, was observed. This result shows similar trend with the results of Dietchs et al. [12].

Steel A contained the largest amount of coarse secondary phase particles (Table 4), which should impair the bendability according to [13]. However, Steel A showed the thickest ferrite layer with a thickness of around 20 μm (Fig. 3a), which must have compensated the negative microstructural features since the bendability. It is also possible that large amount of coarse secondary phase particles in Steel A has increased the randomness of individual tests results, since coarse particles initiate void formation, which in turn facilitate the crack formation in bending. When it comes to grain size effects, the role of very fine PAGS in Steel A did not show clear effect on 3-point bendability. The formation of soft ferrite layer was not as obvious in the other Cr alloyed Steel B, but small amount of polygonal ferrite was observed in optical migrographs (Fig. 3b) and was supported by the measured carbon contents around 0.10 % near the surface (Fig. 4). The behavior of this steel was logical: larger post-uniform elongation values correlated with the improved 3-point bendability.

When it comes to the Mo alloyed steels, Steel C showed also small amount of ferritic phases on the surface (Fig. 3c) resulting from the decarburization (Fig. 4c) that was comparable with Steel A. A small improvement in α_{Fmax} was observed after the BH treatment, which is not totally consistent with the clear increments in post-uniform elongation values. However, the positive trend is expected. Another Mo alloyed Steel D, in turn, did not show any signs of ferrite on the subsurface region (Fig. 3d). In addition, the carbon content of the subsurface region was measured to be the highest, i.e., around 0.15-0.20 % (Fig. 4). Regarding the clearly improved ductility of Steel D in the PH+BH condition (Table 5), the negative correlation between post-uniform elongation and α_{Fmax} is very contradictory. One of the possible reasons could be the detrimental effect of upper bainite mentioned in [58]. The presence of upper bainite could explain the negligible effect of the BH treatment in Steel D, but more systematic investigations would be needed to confirm this.

In the case of Steel E, a thin ferritic decarburization layer was formed during the austenitizing. This observation was supported by the measured carbon contents, i.e., around 0.05 % near the surface (Fig. 4). Based on the present results and alloy compositions (Table 1), the absence of boron in Steel E must have also promoted the formation of ferrite in comparison with Steel D. Steel E showed analogous behavior with Steel B (Fig. 14a), and contained the smallest amount of coarse inclusions (Table 3) as well as slightly thicker decarburization layer compared to Steel B (Fig. 3 and Fig. 4). Irrespective to larger PAGS (Table 2), the bendability of Steel E was the best and the positive effect of the BH treatment was the strongest. Also this confirms that the PAGS refinement seems to be only secondary factor controlling the 3-point bendability of uncoated 34MnB5 based steels, at least within the range of the PAGS attained in the present study. A small total amount of inclusions (sum of nano-sized incoherent precipitates and coarse inclusions) was common in Steels B and E, and is thus worthy of a brief discussion. Regarding this, Steninger and Melander [59] pointed out that the total volume fraction

of inclusions determine the ductility in bending deformation. Also a recent study of Hutchinson et al. [20] support the same idea: the scientists found out that the elimination of TiN and AlN improved maximum bending angle of non-boron alloyed martensitic steels deoxidized using Si instead of Al. When it comes to the formation of coarse inclusions, Steel E had a very similar alloying concept (Table 3) and showed superior bendability in particular after the BH treatment (Fig. 14a).

5. Conclusions

Microstructure-property relationships of five 34MnB5 based press hardening steels were analyzed by focusing on the role of micro alloying elements Ti and V when combined with hardenability increasing alloying elements Cr or Mo. In addition, the effects of bake hardening treatment of 170 ˚C (423 K)/20 min was investigated. The main outcomes of this work can be concluded as follows:

(1) Prior austenite grain size (PAGS) refinement was achieved with both Ti (0.09 %) and V (~ 0.15 %), but micro alloying with Ti resulted in more efficient refining effect. However, it was discovered that also initial microstructure controls the PAGS and should be taken into account in 34MnB5 based steels. In addition, a correlation between PAGS, size of micro alloy precipitates, and yield ($R_{p0.2}$) and tensile strength values (R_m) of die-quenched martensitic steels was observed. Nevertheless, the industrially attainable increase in strength via the PAGS refinement was found to be only some tens of MPa.

(2) The simulated BH treatment of 170 ˚C (423 K)/20 min had a clear effect on the mechanical properties by increasing $R_{p0.2}$ and post-uniform elongation, but decreasing R_m values due to tempering of martensite. These results suggest that the BH treatment provides a valuable possibility for fine-tuning

816 the properties of 34MnB5 type steels. The measured BH effect showed dependency on the alloying
817 concept since it is controlled by PAGS as well as amount and type of micro alloy precipitates.
818
819 (3) A 34MnB5 based non-boron alloyed steel (Steel E), with the alloying concept of 0.3 Mo-0.15 V-
820 0.0060 N (wt-%), exhibited a distinct BH behavior after the short austenitizing cycle of A_{c3}+60 s (~ 180
821 s) at 900 ˚C (1173 K). Whereas the attained increase in $R_{p0.2}$ of the other investigated steels was 170
822 MPa on average, the value of Steel E was 300 MPa, respectively. In addition, the decrease in R_m was
823 exceptionally low, i.e., 20 MPa compared to 130 MPa measured for other steels on average. However,
824 the values of Steel E decreased to 170 MPa and 60 MPa, respectively, in the case of longer
825 austenitization cycle of A_{c3}+180 s (~ 5 min) at 900 ˚C (1173 K). It is suggested that the behavior of Steel
826 E (A_{c3}+60 s) could be only explained with the presence of coherent V(C,N) precipitates. Hence, the
827 coherency is easily lost with the longer austenitization times and temperatures.
828
829 (4) In a genera level, the measured bending angles at maximum force (α_{Fmax}) were promising, i.e., 55-
830 62˚ in the die-quenched condition. The values increased generally to 57-73˚ as a result of the BH
831 treatment. However, clear improvements were observed only for two V micro alloyed steels (Steels C
832 and E) with the alloying concepts of 0.3 Cr-0.15 V-0.03 Al-0.02 Ti-0.0020 B and 0.3 Mo-0.15 V-0.0060
833 N (without Al-Ti-B additions) (wt-%), even though the improved ductility in terms of post-uniform
834 elongation was generally observed for all steels. Therefore, several factors, i.e., local cooling rate,
835 fraction of secondary phase particles, and subsurface microstructure need to be taken into account when
836 evaluating 3-point bendability of PHS with different chemical compositions.
837
838 (5) The largest bending angle at the maximum force (α_{Fmax}=73˚), was achieved for Steel E after the BH
839 treatment. This steel had a thin ferritic layer (10-15 μm) on the surface and the fraction of coarse

840 inclusions was the smallest. Based on this, it is suggested that increased plasticity of martensite (BH
841 treatment), local plasticity of subsurface region (soft ferritic layer on the surface), reduced risk for void
842 formation (minimized amount of coarse particles/inclusions), and fine PAGS (resistance against crack
843 propagation) result in the superior 3-point bendability.
844
845 (6) Despite some discrepancies in the 3-point bending results, it is concluded that both Cr and Mo can be
846 used to control the hardenability of 34MnB5 type steels without significant differences in the
847 mechanical properties. Regarding the PAGS refinement, V may be preferred above Ti, since
848 hyperstoichiometric amounts of Ti tends to increase the amount of coarse secondary phase particles such
849 as $Ti_4C_2S_2$. However, the lower stability of V based carbides requires appropriate control of the
850 austenitization parameters.
851
852 **Acknowledgements:**
853
854 We want to thank Johan Lönnqvist and Christer Eggertson (Swerea KIMAB) for carrying out laboratory
855 melts, Jussi Paavola (University of Oulu) for performing laboratory rolling of experimental steels, and
856 Sanna Järn (SSAB Europe Oy) for implementing GDOES analysis. This study was financially supported
857 by the Finnish Funding Agency for Technology and Innovation (Tekes) in the Breakthrough Steels and
858 Applications Program of the Finnish Metals and Engineering Competence Cluster (FIMECC Ltd), which
859 is gratefully acknowledged. The author wants to thank Tampere University of Technology (TUT's
860 Graduate School), Emil Aaltonen Foundation, and Finnish Foundation for Technology Promotion for
861 financial support.
862
863
864

References

[1] K. Mori, P.F. Bariani, B.-A. Behrens, A. Brosius, S. Bruschi, T. Maeno, M. Merklein, J. Yanagimoto, *CIRP Ann.-Manuf. Techn*. vol. 66, no. 2, 2017, pp.755-777.

[2] T. Gerber, I. Heckelmann, N. Vives Diaz, F.-J. Lenze, Efforts in Expanding the Portfolio of Hot Forming Steel Material Concepts, in: M. Oldenburg, P. Prakash, K. Steinhoff, (Eds.), *Proc. 4th International Conference on Hot Sheet Metal Forming of High-Performance Steel*, Luleå, 2013, pp. 145-152.

[3] G. Krauss, *Mater. Sci. Eng. A*, vol. 273–275, 1999, pp. 40-57.

[4] M. Naderi, Hot Stamping of Ultra High Strength Steels, Doctoral Thesis, University of Aachen, 2007.

[5] H. Mohrbacher, Influence of Alloy Modifications and Microstructure on Properties and Crash Performance of Press Hardened Steel Components, in: M. Oldenburg, P. Prakash, K. Steinhoff, (Eds.), *Proc. 6th International Conference on Hot Sheet Metal Forming of High-Performance Steel*, Atlanta, 2017, pp. 213-220.

[6] A. Tokizawa, K. Yamamoto, Y. Takemoto, T. Senuma, Development of 2000MPa Class Hot Stamped Steel Components with Good Toughness and High Resistance against Delayed Fracture, in: M. Oldenburg, P. Prakash, K. Steinhoff, (Eds.), *Proc. 4th International Conference on Hot Sheet Metal Forming of High-Performance Steel*, Luleå, 2013, pp. 473-479.

[7] P. Larour, H. Pauli, T. Kurz, T. Hebesberger, Influence of post uniform tensile and bending properties on the crash behaviour of AHSS and press-hardening steel grades, in: *Proc. of the Annual Conference of the International Deep Drawing Research Group (IDDRG 2010)*, Graz, 2010.

[8] J. Bian, L. Wang, H. Mohrbacher, H.Z. Lu, W.J. Wang, *Adv. Mater. Res*., vol. 1063, 2015, pp. 7-20.

[9] T. Kurz, P. Larour, J. Lackner, T. Steck, G. Jesner, Press-hardening of zinc coated steel – characterization of a new material for a new process, , in: E. Till et al. (Ed.), *Proc. Annual Conference of the International Deep Drawing Research Group (IDDRG 2016)*, Linz, 2016, pp. 414-427.

[10] D. Fan, H. Kim, B. De Cooman, *Steel Res. Int*., vol. 80, no. 3, 2009, pp. 241-248.

[11] H. Järvinen, M. Honkanen, M. Järvenpää, P. Peura, *J. Mater. Process. Tech*., vol. 252, 2018, pp. 90-104.

[12] P. Dietsch, K. Tihay, S. Cobo, S. Sarkar, D. Hasenpouth, D. Cornette, Predictive Approach for Crash Performance of Press Hardened Steels and its Application on New Product Developments, in: M. Oldenburg, P. Prakash, K. Steinhoff, (Eds.), *Proc. 6th International Conference on Hot Sheet Metal Forming of High-Performance Steel*, Atlanta, 2017, pp. 629-638.

[13] J. Bian, H. Lu, W. Wang, A. Guo, Metallurgical Solutions to Improve Bending and Crash Performance of Press Hardening Steels, in: M. Oldenburg, P. Prakash, K. Steinhoff, (Eds.), *Proc. 6th*

International Conference on Hot Sheet Metal Forming of High-Performance Steel, Atlanta, 2017, pp. 600-609.

[14] J. Wang, Y. Liu, Q. Lu, J. Pang, Z. Wang, C.M. Enloe, J.P. Singh, C.D. Horvath, Effect of Microstructure on Impact Toughness of Press Hardening Steels with Tensile Strength above 1.8GPa, in: M. Oldenburg, P. Prakash, K. Steinhoff, (Eds.), *Proc. 6th International Conference on Hot Sheet Metal Forming of High-Performance Steel*, Atlanta, 2017, pp. 717-727.

[15] W.S. Choi, B.C. De Cooman, *Steel Res. Int.*, vol. 85, no. 5, 2014, pp. 824-835.

[16] J. Bian, H. Mohrbacher, Novel Alloy Desing for Press Hardening Steels with Better Crash Performance, in: *Proc. of AIST International Symposium of New Developments of Advanced High Strength Sheet Steels*, Colorado, USA, pp. 251.

[17] K. Hikida, T. Nishibata, H. Kikuchi, T. Suzuki, N. Nakayama, Properties of New TS 1800 MPa Grade Hot Stamping Steel and Application for Bumber Beam, in: K. Steinhoff, M. Oldenburg, P. Prakash, (Eds.), *Proc. 5th International Conference on Hot Sheet Metal Forming of High-Performance Steel*, Toronto, 2015, pp. 127-134.

[18] M. Maikranz-Valentin, Technological Properties of Conventional and Optimized Press-Hardening Steels, in: M. Oldenburg, P. Prakash, K. Steinhoff, (Eds.), *Proc. 6th International Conference on Hot Sheet Metal Forming of High-Performance Steel*, Atlanta, 2017, pp. 317-324.

[19] S. Otani, M. Kozuka, T. Murakami, J. Naito, A. Pichler, T. Kurz, Metallurgical Controlling Factors for the Ductility of Hot Stamped Parts, in: K. Steinhoff, M. Oldenburg, P. Prakash, (Eds.), *Proc. 5th International Conference on Hot Sheet Metal Forming of High-Performance Steel*, Toronto, 2015, pp. 411-416.

[20] B. Hutchinson, D. Martin, O. Karlsson, F. Lindberg, H. Thoors, R.K.W. Marceau, A.S. Taylor, *Mater. Sci. Tech.*, vol. 33, No. 4, 2017, pp. 497-506.

[21] M. Matsumoto, Y. Takemoto, T. Senuma, Influence of Microstructures on Hydrogen Embrittlement Susceptibility of Hot Stamped Ultrahigh Strength Components, in: K. Steinhoff, M. Oldenburg, P. Prakash, (Eds.), *Proc. 5th International Conference on Hot Sheet Metal Forming of High-Performance Steel*, Toronto, 2015, pp. 55-63.

[22] T. Kishimoto, Y. Takemoto, T. Senuma, Influence of Nb and Mn Content on Resistance to Delayed Fracture of Ultrahigh Strength Hot Stamped Steel Sheets, in: M. Oldenburg, P. Prakash, K. Steinhoff, (Eds.), *Proc. 6th International Conference on Hot Sheet Metal Forming of High-Performance Steel*, Atlanta, 2017, pp. 187-194.

[23] H. Asahi, *ISIJ Int.*, vol. 42, No. 10, 2002, pp. 1150-1155.

[24] F. Han, B. Hwang, D. Suh, Z. Wang, D.L. Lee, S. Kim, *Met. Mater. Int.*, vol. 14, No. 6, 2008, pp. 667.

[25] W.T. Geng, A.J. Freeman, G.B. Olson, *Phys. Rev. B*, vol. 63, no. 16, 2001, pp. 165415.

935 [26] H. Kitahara, R. Ueji, N. Tsuji, Y. Minamino, *Acta Mate*r., vol. 54, no. 5, 2006, pp. 1279-1288.

936 [27] T.N. Baker, *Ironmaking & Steelmaking*, vol. 43, no. 4, 2016, pp. 264-307.

937 [28] D.K. Matlock, J.G. Speer, *Mater. Sci. Tech*., vol. 25, No. 9, 2009, pp. 1118-1125.

938 [29] S.-C. Wang, P.-W. Kao, *J. Mater. Sci*., vol. 28, no. 19, 1993, pp. 5169-5175.

939 [30] D. Glisic, N. Radovic, A. Koprivica, A. Fadel, D. Drobnjak, *ISIJ Int*., vol. 50, 2010, pp. 601-606.

940 [31] H. Järvinen, M. Isakov, T. Nyyssönen, M. Järvenpää, P. Peura, *Mater. Sci. Eng. A*, vol. 676, 2016,
941 pp. 109-120.

942 [32] O.G. Kasatkin, B.B. Vinokur, V.L. Pilyushenko, *Met. Sci. Heat Treat*+, vol. 26, no. 1, 1984, pp.
943 27-31.

944 [33] EN 10325:2006, Steel. Determination of yield strength increase by the effect of heat treatment
945 (Bake-Hardening-Index), BSI, 2006.

946 [34] T. Nyyssönen, M. Isakov, P. Peura, V.-T. Kuokkala, *Metall. Mater. Trans. A*, vol. 47, no. 6, 2016,
947 pp. 2587-2590.

948 [35] ImageJ (Image Processing and Analysis in Java), https://imagej.nih.gov/ij/index.html. Accessed 24
949 May 2018.

950 [36] VDA 238-100 test specification draft: Plate bending test for metallic materials, 12/2010.

951 [37] T. Nishibata, N. Kojima, *J. Alloy Compd*., vol. 577, No. 0, 2013, pp. 549-554.

952 [38] G. Krauss, *ISIJ Int*., vol. 35, No. 4, 1995, pp. 349-359.

953 [39] W.S. Choi, J. Lee, B.C. De Cooman, *Mater. Sci. Eng. A*, vol. 639, 2015, pp. 439-447.

954 [40] R. Soto, W. Saikaly, X. Bano, C. Issartel, G. Rigaut, A. Charai, *Acta Mater*., vol. 47, no. 12, 1999,
955 pp. 3475-3481.

956 [41] Y. Han, J. Shi, L. Xu, W.Q. Cao, H. Dong, *Mater. Design*, vol. 34, 2012, pp. 427-434.

957 [42] S. Aminorroaya, R. Dippenaar, *J. Microsc.-Oxford*, vol. 232, 2008, pp. 123-9.

958 [43] T. Gladman, *The physical Metallurgy of Microalloyed Steels*, The Institute of Materials, London,
959 1997, pp. 81-211.

960 [44] R. Lagneborg, T. Siwecki, S. Zajac, B. Hutchinson, *Scand. J. Metall*., vol. 28, 1999, pp. 186-241.

961 [45] Y. Funakawa, T. Shiozaki, K. Tomita, T. Yamamoto, E. Maeda, *ISIJ Int*., vol. 44, no. 11, 2004, pp.
962 1945-1951.

963 [46] S. Zajac, T. Siwecki, W.B. Hutchinson, R. Lagneborg, *ISIJ Int*., vol. 38, no. 10, 1998, pp. 1130-
964 1139.

965 [47] S.-I. Tabata, K. Hikida, K. Kusumi, Effect of Cooling Rate below the Martensite Start Temperature
966 on the Yield of a Hot-Stamped Steel Sheet, in: M. Oldenburg, P. Prakash, K. Steinhoff, (Eds.), *Proc. 6th*
967 *International Conference on Hot Sheet Metal Forming of High-Performance Steel*, Atlanta, 2017, pp.
968 299-307.

969 [48] E.I. Galindo-Nava, P.E.J. Rivera-Díaz-del-Castillo, *Acta Mater*., vol. 98, 2015, pp. 81-93.

970 [49] B. Ju, H. Wu, D. Tang, N. Dang, *J. Iron Steel Res. Int*., vol. 23, no. 5, 2016, pp. 495-500.

971 [50] E.I. Galindo-Nava, P.E.J. Rivera-Díaz-del-Castillo, *Scripta Mater*., vol. 110, 2016, pp. 96-100.

972 [51] M. Maikranz-Valentin, U. Weidig, U. Schoof, H.-H. Becker, K. Steinhoff, *Steel Res. Int*., vol. 79,
973 no. 2, 2008, pp. 92-97.

974 [52] M. Saeglitz, G. Krauss, *Metall. Mater. Trans. A*, vol. 28, no. 2, 1997, pp. 377-387.

975 [53] S.C. Kennett, G. Krauss, K.O. Findley, *Scripta Mater*., vol. 107, 2015, pp. 123-126.

976 [54] A.G. Kostryzhev, A. Al Shahrani, C. Zhu, J.M. Cairney, S.P. Ringer, C.R. Killmore, E.V.
977 Pereloma, *Mater. Sci. and Eng. A*, vol. 607, 2014, pp. 226-235.

978 [55] W.C. Leslie, R. Sober, *ASM Trans Quart*, vol. 60, no. 1, 1967, pp. 99-111.

979 [56] D.H. Sulistiyo, L. Cho, E.J. Seo, B.C. De Cooman, *Mater. Sci. Tech*., 2016, pp. 1-14.

980 [57] A. Saastamoinen, A. Kaijalainen, D. Porter, P. Suikkanen, *Mater. Charact*. vol. 134, 2017, pp. 172-
981 181.

982 [58] A.J. Kaijalainen, P.P. Suikkanen, L.P. Karjalainen, D.A. Porter, *Mater. Sci. Eng. A*, vol. 654, 2016,
983 pp. 151-160.

984 [59] J. Steninger, A. Melander, *Scand. J. Metall*., vol. 11, no. 2, 1982, pp. 55-71.

985

Table 1. Codes and chemical compositions (in wt-%) for the investigated steels.

Steel	Sheet thickness	C %	Si %	Mn %	Cr %	Mo %	V %	Ti %	Al %	B %	N %	Ti/N ratio
Ref	1.1 mm	0.35	0.26	1.30	0.15	0.01	0	0.029	0.033	0.0026	0.0033	8.8
A	1.5 mm	0.35	0.30	1.37	0.30	0	0	0.090	0.023	0.0022	0.0029	31.0
B	1.5 mm	0.34	0.30	1.37	0.30	0	0.144	0.020	0.024	0.0019	0.0036	5.6
C	1.5 mm	0.34	0.29	1.38	0.02	0.29	0	0.019	0.021	0.0019	0.0017	11.2
D	1.5 mm	0.34	0.30	1.36	0.02	0.30	0.146	0.020	0.028	0.0017	0.0033	6.1
E	1.5 mm	0.34	0.29	1.28	0.02	0.30	0.147	0.001	0.004	0.0001	0.0060	0.2

Table 2. Calculated A_{c3} temperatures and examined austenitization cycles of the press hardening experiments based on the time required to reach A_{c3} at a constant furnace temperature of 900 ˚C (1173 K).

Steel	A_{c3}	A_{c3}+60 s (~ 3 min)	A_{c3}+180 s (~ 5 min)
Ref	800 ˚C (1073 K)	172 s	292 s
A	812 ˚C (1085 K)	178 s	298 s
B	797 ˚C (1070 K)	172 s	292 s
C	813 ˚C (1086 K)	179 s	299 s
D	815 ˚C (1088 K)	180 s	300 s
E	809 ˚C (1082 K)	177 s	297 s

Table 3. Measured PAGS for the PH samples austenitized for A_{c3}+60 s and A_{c3}+180 s at 900 ˚C (1173 K). Designation ΔGS refers to the increase in PAGS between the studied austenitization cycles.

Steel	PAGS, (µm) – TD, A_{c3}+60s/900 °C	PAGS (µm) – TD, A_{c3}+180s/900 °C	ΔGS(µm) – TD
Ref	4.7 (±0.4)	5.6 (±0.7)	0.9
A	2.4 (±0.1)	3.8 (±0.3)	1.4
B	3.7 (±0.4)	5.4 (±0.6)	1.7
C	3.6 (±0.4)	4.5 (±0.6)	0.9
D	2.8 (±0.2)	3.9 (±0.4)	1.1
E	2.6 (±0.2)	6.0 (±0.8)	3.4

Table 4. Types and determined area fractions of coarse secondary phase particles.

Steel	Coarse secondary phase particles/inclusions based on SEM-EDS (+oxides and oxysulfides)	Calculated area fractions (%)		
		A_{c3}+60 s	A_{c3}+180 s	Total (avg.)
Ref	MnS; TiN; Al_2O_3+TiN, Ti(C,N)	0.094	0.065	0.080
A	MnS; Al_2O_3; TiN; Al_2O_3+TiN; $Ti_4C_2S_2$; TiC; Ti(C,N)	0.172	0.169	0.171
B	MnS; Al_2O_3; TiN; (Ti,V)N, Al_2O_3+(Ti,V)N; (Ti, Vn)(C,N)	0.068	0.080	0.074
C	MnS; Al_2O_3; TiN; TiN+Al_2O_3;	0.087	0.082	0.085
D	MnS; Al_2O_3; TiN, (Ti,V)N; Al_2O_3+(Ti,V)N; (V,Ti,Mo)C; (V,Ti,Mo)(C,N)	0.080	0.093	0.087
E	MnS; Al_2O_3	0.061	0.064	0.063

Table 5. Mechanical properties for the investigated steels in both PH and PH+BH conditions. Post-uniform elongation values are only used for the comparison between the investigated steels.

	A_{c3}+60 s/900 °C (1173 K) - PH					A_{c3}+60 s/900 °C (1173 K) - PH+BH				
Steel	$R_{p0.2}$ (MPa)	R_m (MPa)	$R_{p0.2}/R_m$	A_g (%)	Post-uniform elongation (%)	$R_{p0.2}$ (MPa)	R_m (MPa)	$R_{p0.2}/R_m$	A_g (%)	Post-uniform elongation (%)
Ref	1480	2120	0.70	5.4	2.0	1620	1960	0.83	4.8	7.2
A	1370	2000	0.69	5.1	2.6	1530	1850	0.83	4.1	5.3
B	1350	1990	0.68	5.2	4.7	1500	1860	0.81	4.7	9.5
C	1320	1980	0.67	5.3	5.4	1510	1870	0.81	4.4	7.1
D	1360	1990	0.68	4.9	5.5	1560	1890	0.83	4.4	7.4
E	1340	1980	0.68	4.6	1.4	1640	1960	0.84	4.5	7.2

	A_{c3}+180 s/900 °C (1173 K) - PH					A_{c3}+180 s/900 °C (1173 K) - PH+BH				
Steel	$R_{p0.2}$ (MPa)	R_m (MPa)	$R_{p0.2}/R_m$	A_g (%)	Post-uniform elongation (%)	$R_{p0.2}$ (MPa)	R_m (MPa)	$R_{p0.2}/R_m$	A_g (%)	Post-uniform elongation (%)
Ref	1460	2120	0.69	5.4	2.6	1550	1950	0.79	4.8	7.2
A	1320	1950	0.68	4.3	2.6	1490	1840	0.81	4.3	7.5
B	1300	1940	0.67	4.4	4.7	1440	1840	0.78	4.9	8.3
C	1290	1940	0.67	4.8	4.6	1430	1810	0.79	4.3	7.7
D	1330	1960	0.68	4.7	3.9	1480	1840	0.80	4.7	10.9
E	1300	1910	0.68	3.7	2.3	1470	1850	0.79	4.2	6.2

Fig. 1. Optical micrographs transverse to the rolling direction of the investigated steels; a) Ref; b) Steel A; c) Steel B; d) Steel C; e) Steel D; f) Steel E.

Fig. 2. Example SEM micrographs of Steel C in; a) PH and; b) PH+BH condition and Steel E in; c) PH and; d) PH+BH condition after austenitizing for A_{c3}+180 s at 900 ˚C (1173 K). The microstructures are mixtures of hard martensite (M) and auto-tempered martensite (AM).

Fig. 3. Optical micrographs from the subsurface regions of the PH steels; a) Steel A; b) Steel B; c) Steel C; d) Steel D; e) Steel E after austenitizing for A_{c3}+180 s at 900 ˚C (1173 K). Steels A, B, C and E show ferritic phases on the surface, whereas the subsurface microstructure of Steel D is most preferably fully martensitic. The scale is the same in all images.

Fig. 4. Carbon concentration profiles; a) measurement #1; b) measurement #2 by GDOES for the laboratory Steels A-D measured from the surface of the 3-point bending samples (A_{c3}+180 s/900 ˚C (1183 K)) in the PH condition.

Fig. 5. Prior austenite grain boundary (PAGB) maps for Steel A austenitized for; a) A_{c3}+60 s; b) A_{c3}+180 s/900 ˚C (1173 K) and for Steel B austenitized for; c) A_{c3}+60 s; d) A_{c3}+180 s/900 ˚C (1173 K). The viewing direction is transverse to the original rolling direction. PAGB are superimposed on EBSD band contrast images as black lines, and the red and green lines show packet and block boundaries of martensite, respectively. (For interpretation of the references to color in this figure legend, the reader is referred to the web version of this article.)

Fig. 6. Example SEM images of; a) Ref; b) Steel A; c) Steel C revealing secondary phase particles as darker from the brighter matrix.

Fig. 7. Results of TEM-analysis (carbon extraction replicas) for the Cr alloyed steels. Steel A in the PH condition after austenitizing for; a) A_{c3}+60 s; b) A_{c3}+180 s at 900 ˚C (1173 K). Respectively, results of Steel B after austenitizing for; c) A_{c3}+60 s; d) A_{c3}+180 s.

Fig. 8. Results of TEM-analysis (carbon extraction replicas) for Mo alloyed steels: Steel D in the PH condition after austenitizing for a) A_{c3}+60 s; b) A_{c3}+180 s at 900 ˚C (1173 K). Respectively, results of Steel E after austenitizing for; c) A_{c3}+60 s; d) A_{c3}+180 s.

Fig. 9. Tensile test curves for Steel D in the case of both austenitization cycles of; a) A_{c3}+60 s; b) A_{c3}+180 s at 900 ˚C (1173 K). The curves measured in both press-hardened (PH) and additionally bake hardened (PH+BH) conditions are presented. The peaks of the curves indicating uniform elongation and ultimate tensile strenght are marked using black circles.

Fig. 10. a) Results of 3-point bending tests expressed as maximum bending angle at maximum force (α_{Fmax}) for the laboratory Steels A-E in both PH and PH+BH conditions. b) Examples of load vs. displacement curves.

Fig. 11. a) Correlation between yield strength ($R_{p0.2}$) and prior austenite grain size (PAGS). b) Correlation between tensile strength (R_m) and PAGS. c) Correlation between precipitate size (micro alloyed Steels A, B, D, and E) and PAGS. Results of Ref are omitted due to smaller sheet thickness.

Fig. 12. a) Correlation between the attained increase in yield strength ($\Delta R_{p0.2}$) and parent austenite grain size (PAGS) after the bake hardening (BH) treatment. b) Correlation between the attained decrease in tensile strength ($-\Delta R_m$) and PAGS, respectively. c) Correlation between $\Delta R_{p0.2}$ and precipitate size. The graph shown in b) presents only the results of micro alloyed Steels A, B, D, and E. Results of Ref are omitted due to smaller sheet thickness.

Fig. 13. Correlation between the area fraction of coarse secondary phase particles and post-uniform elongation in; a) press-hardened (PH) condition; b) press-hardened and additionally bake hardened (PH+BH) condition.

Fig. 14. a) Correlation between post-uniform elongation and 3-point bendability for PH and PH+BH treated laboratory Steels A-E. b) 3-point bending data (5 parallel tests) for a reference grade, ZnFe coated 22MnB5 in both PH and PH+BH conditions after corresponding austenitizing cycle of A_{c3}+180 s at 900 ˚C (1173 K).